

Title: Identification of lectin receptors for conserved SARS-CoV-2 glycosylation sites

Authors: David Hoffmann^{1*}, Stefan Mereiter^{1*}, Yoo Jin Oh², Vanessa Monteil³, Rong Zhu², Daniel Canena², Lisa Hain², Elisabeth Laurent⁴, Clemens Grünwald-Gruber⁵, Maria Novatchkova¹, Melita Ticevic¹, Antoine Chabloz⁶, Gerald Wirnsberger⁷, Astrid Hagelkruys¹, Friedrich Altmann⁵, Lukas Mach⁸, Johannes Stadlmann^{1,5}, Chris Oostenbrink⁹, Ali Mirazimi^{3,10}, Peter Hinterdorfer² and Josef M. Penninger^{1,6#}

Affiliations:

¹ IMBA, Institute of Molecular Biotechnology of the Austrian Academy of Sciences; 1030, Vienna; Austria

² Institute of Biophysics, Johannes Kepler University Linz, Gruberstr. 40, 4020 Linz, Austria

³ Karolinska Institute and Karolinska University Hospital, Department of Laboratory Medicine, Unit of Clinical Microbiology, 17177 Stockholm, Sweden

⁴ Department of Biotechnology and BOKU Core Facility Biomolecular & Cellular Analysis, University of Natural Resources and Life Sciences, Muthgasse 18, 1190, Vienna, Austria

⁵ Department of Chemistry, University of Natural Resources and Life Sciences, Muthgasse 18, 1190 Vienna, Austria

⁶ Department of Medical Genetics, Life Science Institute, University of British Columbia, Vancouver, Canada

⁷ Apeiron Biologics, Campus Vienna Biocenter 5, 1030 Vienna, Austria

⁸ Department of Applied Genetics and Cell Biology, University of Natural Resources and Life Sciences, Muthgasse 18, 1190 Vienna, Austria

⁹ Institute for Molecular Modeling and Simulation, Department for Material Sciences and Process Engineering, University of Natural Resources and Life Sciences, Muthgasse 18, 1190 Vienna, Austria

¹⁰ National Veterinary Institute, 751 89 Uppsala, Sweden

* These authors contributed equally to this work

Correspondence to: josef.penninger@ubc.ca

35 **Abstract:** New SARS-CoV-2 variants are continuously emerging with critical
36 implications for therapies or vaccinations. All 22 N-glycan sites of SARS-CoV-2 Spike
37 remain highly conserved among the variants B.1.1.7, 501Y.V2 and P.1, opening an
38 avenue for robust therapeutic intervention. Here we used a comprehensive library of
39 mammalian carbohydrate-binding proteins (lectins) to probe critical sugar residues on
40 the full-length trimeric Spike and the receptor binding domain (RBD) of SARS-CoV-2.
41 Two lectins, Clec4g and CD209c, were identified to strongly bind to Spike. Clec4g and
42 CD209c binding to Spike was dissected and visualized in real time and at single
43 molecule resolution using atomic force microscopy. 3D modelling showed that both
44 lectins can bind to a glycan within the RBD-ACE2 interface and thus interferes with
45 Spike binding to cell surfaces. Importantly, Clec4g and CD209c significantly reduced
46 SARS-CoV-2 infections. These data report the first extensive map and 3D structural
47 modelling of lectin-Spike interactions and uncovers candidate receptors involved in
48 Spike binding and SARS-CoV-2 infections. The capacity of CLEC4G and mCD209c
49 lectins to block SARS-CoV-2 viral entry holds promise for pan-variant therapeutic
50 interventions.

51 **Introduction:** COVID-19 caused by SARS-CoV-2 infections has triggered a pandemic
52 massively disrupting health care, social and economic life. SARS-CoV-2 main entry
53 route into target cells is mediated by the viral Spike protein, which binds to angiotensin
54 converting enzyme 2 (ACE2) expressed on host cells (Monteil et al., 2020). The Spike
55 protein is divided into two subunits, S1 and S2. The S1 subunits comprises the
56 receptor binding domain (RBD) which confers ACE2 binding activity. The S2 subunit
57 mediates virus fusion with the cell wall following proteolytic cleavage (Hoffmann et al.,
58 2020; Shang et al., 2020; Walls et al., 2020). Cryo-electron microscopy studies have
59 shown that the Spike protein forms a highly flexible homotrimer containing 22 *N*-
60 glycosylation sites each, 18 of which are conserved with the closely related SARS-
61 CoV which caused the 2002/03 SARS epidemic (Ke et al., 2020; Walls et al., 2020).
62 Point mutations removing glycosylation sites of the SARS-CoV-2 Spike protein were
63 found to yield less infectious pseudo-typed viruses (Li et al., 2020). As Spike and RBD
64 glycosylation affect ACE2 binding and SARS-CoV-2 infections, targeting virus specific
65 glycosylation could be a novel means for therapeutic intervention.

66

67 Glycosylation of viral proteins ensures proper folding and shields antigenic viral
68 epitopes from immune recognition (Watanabe et al., 2020b; Watanabe et al., 2019).
69 To create this glycan shield, the virus hijacks the host glycosylation machinery and
70 thereby ensures the presentation of self-associated glycan epitopes. Apart from
71 shielding epitopes from antibody recognition, glycans can be ligands for lectin
72 receptors. For instance, mannose-specific mammalian lectins, like DC-SIGN (CD209)
73 or its homolog L-SIGN (CD299), are well known to bind to viruses like HIV-1 and also
74 SARS-CoV (Van Breedam et al., 2014). Lectin receptors are often expressed on
75 immune and endothelial cells and serve as pattern recognition receptors involved in

76 virus internalization and transmission (Osorio and Reis e Sousa, 2011). Recent
77 studies have characterized the recognition of the SARS-CoV-2 Spike by previously
78 known virus-binding lectins, such as DC-SIGN, L-SIGN, MGL and MR (Gao et al.,
79 2020). Given that SARS-CoV-2 relies less on oligo-mannose-type glycosylation, as
80 compared to for instance HIV-1, and displays more complex-type glycosylation, it is
81 unknown if additional lectin receptors are capable of binding the Spike protein and
82 whether such interactions might have functional relevance in SARS-CoV-2 infections.

83

84 **Results:**

85 **Preparation of the first near genome-wide lectin library to screen for novel** 86 **binders of Spike glycosylation.**

87 To systematically identify lectins that bind to the trimeric Spike protein and RBD of
88 SARS-CoV-2, we searched for all annotated carbohydrate recognition domains
89 (CRDs) of mouse C-type lectins, Galectins and Siglecs. Of 168 annotated CRDs, we
90 were able to clone, express and purify 143 lectin-CRDs as IgG2a-Fc fusion proteins
91 from human HEK293F cells (Fig. 1A, table S1). The resulting dimeric lectin-Fc fusion
92 proteins (hereafter referred to as lectins) showed a high degree of purity (Fig. 1B). This
93 collection of lectins is, to our knowledge, the first comprehensive library of mammalian
94 CRDs.

95

96 We next recombinantly expressed monomeric RBD and full-length trimeric Spike
97 protein (hereafter referred to as Spike protein) in human HEK293-6E cells. Using mass
98 spectrometry, we characterized all 22 *N*-glycosylation sites on the full-length Spike
99 protein and 2 *N*-glycosylation sites on the RBD (Fig. 1C and table S2). Most of the
100 identified structures were in accordance with previous studies using full-length Spike

101 (Watanabe et al., 2020a) with the exception of N331, N603 and N1194, which
102 presented a higher structural variability of the glycan branches (Fig. 1C and table S2).
103 Importantly, the *N*-glycan sites of Spike are highly conserved among the sequenced
104 SARS-CoV-2 viruses including the emerging variants B.1.1.7, 501Y.V2 and P.1 (Fig
105 S1A, B). The detected *N*-glycan species ranged from poorly processed oligo-mannose
106 structures to highly processed multi-antennary complex *N*-glycans in a site-dependent
107 manner. This entailed also a large variety of terminal glycan epitopes, which could act
108 as ligands for lectins. Notably, the two glycosylation sites N331 and N343 located in
109 the RBD carried more extended glycans, including sialylated and di-fucosylated
110 structures, when expressed as an independent construct as opposed to the full-length
111 Spike protein (Fig. 1C and table S2). These data underline the complex glycosylation
112 of Spike and reveal that *N*-glycosylation of the RBD within the 3D context of full-length
113 trimeric Spike is different from *N*-glycosylation of the RBD expressed as minimal ACE2
114 binding domain.

115

116 **CD209c and Clec4g are novel high affinity binders of SARS-CoV-2 Spike.**

117 We evaluated the reactivity of our murine lectin library against the trimeric Spike and
118 monomeric RBD of SARS-CoV-2 using an ELISA assay (Fig. S2A). This screen
119 revealed that CD209c (SIGNR2), Clec4g (LSECTin), and Reg1 exhibited pronounced
120 binding to Spike, whereas Mgl2 and Asgr1 displayed elevated binding to the RBD (Fig.
121 2A, B and table S3). Further, we investigated the reactivity of the lectin library against
122 human recombinant soluble ACE2 (hrsACE2); none of the lectins bound to hrsACE2
123 (Fig. S2B). We excluded Reg1 from further studies due to inconsistent ELISA results,
124 likely due to protein instability. Asgr1 was excluded because it bound only to RBD but
125 not to the Spike trimer, in accordance to the differences in glycosylation of glycosites

126 N331 and N343 between Spike and RBD (Fig. 1C). This highlights the importance of
127 using a full-length trimeric Spike protein for functional studies. To confirm that the
128 observed interactions were independent of protein conformation, Spike was denatured
129 prior to the ELISA assay; binding of CD209c and Clec4g to the unfolded Spike
130 remained unaltered (Fig. 2C). Importantly, enzymatic removal of *N*-glycans by
131 PNGase F treatment reduced the binding of CD209c, Clec4g, and Mgl2 towards Spike
132 (Fig. 2D and Fig. S2C), confirming *N*-glycans as ligands. Binding of ACE2, which relies
133 on protein-protein interactions, was completely abrogated when Spike was denatured
134 (Fig. 2C). These data identify lectins that have the potential to bind to the RBD and
135 trimeric Spike of SARS-CoV-2.

136

137 Based on the robust *N*-glycan dependent Spike binding, we focused our further studies
138 on CD209c and Clec4g. We first used surface plasmon resonance (SPR) to determine
139 the kinetic and equilibrium binding constants of these lectins to the trimeric Spike. The
140 resulting experimental binding curves were fitted to the “bivalent analyte model”
141 (Traxler et al., 2017) which assumes two-step binding of the lectin dimers to adjacent
142 immobilized Spike trimer binding sites (Fig. 2E, F). From these fits, we computed the
143 kinetic association ($k_{a,1}$), kinetic dissociation ($k_{d,1}$), and equilibrium dissociation ($K_{d,1}$)
144 binding constants of single lectin bonds (Table 1). The equilibrium dissociations ($K_{d,1}$)
145 values were 1.6 μ M and 1.0 μ M for Clec4g and CD209c, respectively.

146

147 **Multiple CD209c and Clec4g molecules bind simultaneously to SARS-CoV-2**
148 **Spike and form compact complexes.**

149 To study Spike binding of these two lectins at the single-molecule level, we used
150 atomic force microscopy (AFM) and performed single molecule force spectroscopy

151 (SMFS) experiments. To this end, we coupled trimeric Spike to the tip of the AFM
152 cantilever and performed single-molecule force measurements (Hinterdorfer et al.,
153 1996), by moving the Spike trimer-coupled tip towards the surface-bound lectins to
154 allow for bond formations (Fig. 3A). Unbinding was accomplished by pulling on the
155 bonds, which resulted in characteristic downward deflection signals of the cantilever,
156 whenever a bond was ruptured (Fig. 3B). The magnitude of these vertical jumps
157 reflects the unbinding forces, which were of typical strengths for specific molecular
158 interactions (Rankl et al., 2008). Using this method (Rankl et al., 2008; Zhu et al.,
159 2010), we quantified unbinding forces (Fig. 3C) and calculated the binding probability
160 and the number of bond ruptures between CD209c or Clec4g and trimeric Spike (Fig.
161 3D). Both lectins showed a very high binding probability and could establish up to 3
162 strong bonds with accumulating interaction force strengths reaching 150 pN in total
163 with trimeric Spike (Fig. 3C), with the preference of single and dual bonds (Fig. 3C,
164 3D, Fig. S3A, B, Table 1). Of note, multi-bond formation leads to stable complex
165 formation, in which the number of formed bonds enhances the overall interaction
166 strength and dynamic stability of the complexes. To assess dynamic interactions
167 between single molecules of trimeric Spike and the lectins in real time we used high-
168 speed AFM (Kodera et al., 2010; Preiner et al., 2014). Addition of Clec4g and CD209c
169 led to a volume increase of the lectin/Spike complex in comparison to the trimeric
170 Spike alone; based on the volumes we could calculate that on average 3.2 molecules
171 of Clec4g and 5.2 molecules of CD209c were bound to one Spike trimer (Fig. 3E, Fig.
172 S3C-E and movies S1-4). These data show, in real-time, at single molecule resolution,
173 that mouse Clec4g and CD209c can directly associate with trimeric Spike.

174

175 **The human lectins CD209 and CLEC4G are high affinity receptors for SARS-**
176 **CoV-2 Spike.**

177 Having characterized binding of murine CD209 and Clec4g to Spike, we next
178 assessed whether their closest human homologues, namely human CD209 (hCD209),
179 and human CD299 (hCD299) for murine CD209c, and human CLEC4G (hCLEC4G)
180 for mouse Clec4g, can also bind to full-length trimeric Spike of SARS-CoV-2. hCD209,
181 hCD299, and hCLEC4G indeed exhibited binding to Spike (Fig. 4A), demonstrating
182 conserved substrate specificities. The binding of these human lectins was again
183 independent of Spike folding and abrogated by *N*-glycan removal (Fig. 4A, B). SPR
184 measurements of hCLEC4G and hCD209 bond formation to Spike showed equilibrium
185 dissociation ($K_{d,1}$) values of 0.3 μ M and 2.4 μ M, respectively, in which the high affinity
186 of hCLEC4G is mainly contributed by its rapid kinetic association rate constant (Fig.
187 4C, D and Table 1). In addition, hCD209 and hCLEC4G showed a high binding
188 probability by AFM with the formation of up to 3 bonds per trimeric Spike (Fig. S4A-
189 C). When we monitored the dynamic interactions of the lectins with the Spike using
190 high speed AFM, we observed binding of - on average - 3.5 hCLEC4G and 3.6
191 hCD209 molecules per trimeric Spike (Fig. 4E and Fig. S4D-F). In summary, our data
192 using ELISA, SMFS, surface plasmon resonance, and high-speed atomic force
193 microscopy show that the human lectins CLEC4G and CD209 can bind to trimeric
194 Spike of SARS-CoV-2, in which the overall interaction strength and dynamic stability
195 leads to compact complex formation.

196

197 **CLEC4G sterically interferes with Spike/ACE2 interaction.** We next 3D modelled
198 binding of hCLEC4G and hCD209 to the candidate glycosylation sites present on
199 Spike and how such attachment might relate to the binding of the trimeric Spike protein

200 to its receptor ACE2. hCD209 is known to bind with high affinity to oligo-mannose
201 structures (Guo et al., 2004). The N234 glycosylation site is the only site within the
202 Spike that carries exclusively oligo-mannose glycans with up to 9 mannose residues
203 (Fig. 1C, table S2). 3D modelling revealed that the oligo-mannose glycans on N234
204 are accessible for hCD209 binding on all 3 monomers comprising the trimeric Spike
205 (Fig. 5 and Fig. S5A, B). Superimposition of ACE2 interacting with the RBD and
206 hCD209 binding to N234, showed that the hCD209 binding occurs at the lateral
207 interface of Spike, distant from the RBD (Fig. 5)

208

209 Human CLEC4G and mouse Clec4g, on the other hand, were shown to have a high
210 affinity for complex *N*-glycans terminating with GlcNAc (Pipirou et al., 2011;
211 Powlesland et al., 2008). To further assess the detailed ligand specificity of these two
212 lectins, we performed glycan microarray analyses comprising of 144 different glycan
213 structures. Our analysis revealed a remarkable specificity of both, human CLEC4G
214 and mouse Clec4g, exclusively for *N*-glycans with an unsubstituted GlcNAc β -
215 1,2Man α -1,3Man arm (Fig. 5A, Fig. S6A, B, and Table S4). In addition, our analysis
216 revealed that mouse CD209c exhibits overlapping ligand specificities with murine
217 Clec4g and human CLEC4G, which is in fact distinct from the known binding profile of
218 human CD209. However, unlike Clec4g, CD209c recognized all *N*-glycan structures
219 that displayed terminal unsubstituted GlcNAc residues, independently of the position
220 in the glycan antennae (Fig. 5A, Fig. S6C and Table S4). The *N*-glycan at N343,
221 located within the RBD, is the glycosylation site most abundantly decorated with
222 terminal GlcNAc in Spike (Fig. 1C, table S2), constituting the candidate binding site
223 for murine CD209c and murine and human CLEC4G.

224

225 The terminal GlcNAc glycans on position N343 are accessible for hCLEC4G binding
226 on all 3 Spike monomers, but in contrast to hCD209, hCLEC4G binding interferes with
227 the ACE2/RBD interaction (Fig. 5B, fig. S5C, D). Since murine Clec4g and murine
228 CD209c show strongly overlapping ligand specificities to hCLEC4G, we next modelled
229 binding of these two lectins to the N343 glycan site. As predicted from our data, both
230 murine Clec4g and murine CD209c indeed interfere with the ACE2/RBD interaction
231 (fig. S5E). Thus, whereas hCD209 is not predicted to directly affect ACE2/RBD
232 binding, murine Clec4g, murine CD209c and human CLEC4G binding to the N343
233 glycan impedes Spike binding to ACE2.

234

235 **CD209c and CLEC4G block SARS-CoV-2 infection.**

236 To test our structural models experimentally, we assessed whether these lectins could
237 interfere with Spike binding to the surface of Vero E6 cells, a frequently used SARS-
238 CoV-2 infection model (Monteil et al., 2020). To determine this, we set-up an AFM
239 based method, measuring spike binding activity on Vero E6 cells. Strikingly, as
240 predicted by the structural modelling, we found that hCLEC4G, but not hCD209,
241 significantly interfered with the binding of trimeric Spike to the Vero E6 cell surface
242 (Fig. 6A). Similarly, mouse Clec4g, and importantly also murine CD209c, albeit to a
243 lesser extent, interfered with Spike binding to Vero E6 cells (Fig. 6B). Finally, we tested
244 the ability of these lectins to reduce the infectivity of SARS-CoV-2. In accordance with
245 our model, murine Clec4g and murine CD209c significantly reduced SARS-CoV-2
246 infection of Vero E6 cells (Fig. 6C). Finally, hCLEC4G also significantly reduced
247 SARS-CoV-2 infection of Vero E6 cells (Fig.6D). These data uncover that the lectins
248 CLEC4G and CD209c can interfere with SARS-CoV-2 infections.

249

250 **Discussion**

251 Here we report the results from unbiased screening of a comprehensive mammalian
252 lectin library for potent SARS-CoV-2 Spike binding, identifying mouse CD209c and
253 Clec4g, as well as their human homologs hCD209 and hCLEC4G, as N-glycan
254 dependent Spike receptors. hCD209 has been identified as candidate receptor for
255 SARS-CoV-2 by other groups, and other lectins have been also implicated in cellular
256 interactions with Spike (Gao et al., 2020; Thépaut et al., 2020). CLEC4G has been
257 reported to associate with SARS-CoV (Gramberg et al., 2005), but has not been
258 implicated in SARS-CoV-2 infections. High-speed atomic force microscopy allowed us
259 to directly observe Spike/lectin interactions in real time. Our high-speed AFM data
260 showed that Spike/CLEC4G form more rigid clusters with lower conformational
261 flexibility as compared to the Spike/CD209 complexes in equilibrium conditions. This
262 is in accordance with faster association rates and shorter dissociation paths of
263 CLEC4G as compared to CD209. The experimentally observed association of 3-4
264 CLEC4G molecules with one molecule of the trimeric spike indicates the formation of
265 high affinity bonds to 1-2 glycosylation sites per monomeric subunit of the trimeric
266 Spike.

267 Since glycosylation is not a template driven process, but rather depends on the
268 coordinated action of many glycosyltransferases and glycosidases (Stanley et al.,
269 2015), each glycosylation site can - within some boundaries - carry a range of glycans.
270 As a consequence, the 3 monomers of Spike can harbor different glycans on the same
271 glycosylation site. We identified N343 as the one glycosylation site that is almost
272 exclusively covered with GlcNAc terminated glycans, the ligands of human CLEC4G
273 and mouse Clec4g as well as, based on our new data, mouse CD209c. Given
274 localization of N343 within the RBD, we hypothesized that CLEC4G and mCD209c

275 binding interferes with the RBD-ACE2 interaction. Indeed, we found that murine
276 Clec4g and human CLEC4G, acting as a multi-valent effective inhibitor ($K_i \sim 35 - 70$
277 nM), can functionally impede with Spike binding to host cell membranes, thereby
278 providing a rationale how this lectin can affect SARS-CoV-2 infections. In support of
279 our data, it has recently been reported that a N343 glycosylation mutant exhibits
280 reduced infectivity using pseudo-typed viruses (Li et al., 2020).

281

282 As for murine CD209c, our atomic force microscopy data indicate that CD209c
283 engages in a larger number of interactions per trimeric Spike (~ 5.2), presumably
284 because mCD209c binds to a greater variety of GlcNAc-linkages than Clec4g. This
285 more promiscuous glycan binding of mCD209c might also explain less, albeit
286 significant, inhibition of Spike binding to VeroE6 surface as compared to human and
287 mouse CLEC4G. Interestingly, the efficiency of inhibiting SARS-CoV-2 infection
288 between murine and human CLEC4G and mCD209c remained comparable. As such,
289 the multi-valent binding of CD209c may block SARS-CoV-2 infection not only through
290 direct interference with ACE2 binding, but possibly also via affecting conformational
291 Spike structures or proteolytic cleavage. Of note, while human and mouse CLEC4G
292 as well as mouse CD209c can interfere with RBD-ACE2 binding, human CD209 does
293 apparently not associate with glycans near the RBD and hence does not block Spike
294 binding to cells. This is in agreement to its proposed high affinity oligo-mannosidic
295 ligands, presented at N234, which is localized at a distance to the RBD-ACE2
296 interface.

297

298 Lectins play critical roles in multiple aspects of biology such as immune responses,
299 vascular functions, or as endogenous receptors for various human pathogens. Hence,

300 our library containing 143 lectins will now allow to comprehensively probe and map
301 glycan structures on viruses, bacteria or fungi, as well as during development or on
302 cancer cells, providing novel insights on the role of lectin-glycosylation interactions in
303 infections, basic biology, and disease. For instance, CD209 is expressed by antigen
304 presenting dendritic cells, as well as inflammatory macrophages (Garcia-Vallejo and
305 van Kooyk, 2013) and is known to bind to a variety of pathogens, like HIV and Ebola,
306 but also *Mycobacterium tuberculosis* or *Candida albicans* (Appelmeik et al., 2003).
307 CLEC4G is strongly expressed in liver and lymph node sinusoidal endothelial cells
308 and can also be found on stimulated dendritic cells and macrophages (Dominguez-
309 Soto et al., 2009; Dominguez-Soto et al., 2007). CD299, one of the two homologues
310 of mouse CD209c, which we also identified to possess Spike binding ability, is co-
311 expressed with CLEC4G on liver and lymph node sinusoidal endothelial cells (Liu et
312 al., 2004). Sinusoidal endothelial cells are important in the innate immune response,
313 by acting as scavengers for pathogens as well as antigen cross-presenting
314 cells (Knolle and Wohleber, 2016). Thus, lectin binding to Spike might couple SARS-
315 CoV-2 infections to antiviral immunity, which needs to be further explored. Since viral
316 protein glycosylation depends on the glycosylation machineries of the infected cells
317 which assemble viral particles (Watanabe et al., 2019), slight changes in glycosylation
318 might explain differences in anti-viral immunity and possibly severity of the disease,
319 with critical implications for vaccine designs. Moreover, Spike-binding lectins could
320 enhance viral entry in tissues with low ACE2 expression, thus extending the organ
321 tropism of SARS-CoV-2.

322

323 Intriguingly, all 22 *N*-glycan sites of Spike remain highly conserved among all the
324 predominant SARS-CoV-2 variants, indicating a selection pressure to preserve these

325 sites. Thus, the capacity of CLEC4G and mCD209c lectins to block SARS-CoV-2 viral
326 entry holds promise for pan-variant therapeutic interventions.

327

328 **Material and Methods:**

329 **Identification of proteins containing carbohydrate recognition domains (CRDs).**

330 Mouse lectin sequences were obtained using a domain-based approach. Briefly,
331 proteins with a C-type lectin-like/IPR001304 domain were downloaded from InterPro
332 66.0 and supplemented with proteins obtained in jackhmmer searches using the
333 PF00059.20 lectin C-type domain definition versus the mouse-specific UniProt and
334 Ensembl databases. The collected set of candidate mouse lectins was made non-
335 redundant using nrdb 3.0. The C-type lectin-like regions were extracted from the full-
336 length proteins using the SMART CLECT domain definition with hmmersearch v3.1b2
337 and extended by 5 amino acids on both sides. To reduce redundancy, principal
338 isoforms were selected using appris 2016_10.v24. In addition, the CRD domains for
339 Galectins and Siglecs were added. In case a gene contained more than 1 CRD, all
340 CRDs were cloned separately and differentiated by _1, _2, etc.

341

342 **Cloning of C-type lectin expression vectors.**

343 We used the pCAGG_00_ccb plasmid and removed the toxic ccb element by cleaving
344 the plasmid with BsaI. Thereafter, we inserted a Fc-fusion construct, consisting of the
345 IL2 secretion signal, followed by an EcoRV restriction site, a (GGGS)₃ linker domain
346 and the mouse IgG2a-Fc domain. Subsequently, each identified CRD, was cloned in-
347 frame into the EcoRV site.

348

349 **Transfection and purification of the lectin-mIgG2a fusion proteins.**

350 The CRD containing plasmids were transfected into Freestyle™ 293-F cells. Briefly,
351 the day before transfection, 293-F cells were diluted to 0.7×10^6 cells/ml in 30 ml
352 Freestyle™ 293-F medium and grown at 120 rpm at 37°C with 8% CO₂. The next
353 morning, 2 µl polyethylenimine (PEI) 25K (1mg/ml; Polysciences, 23966-1) per µg of
354 plasmid DNA were mixed with pre-warmed Opti-MEM media (ThermoFisher
355 Scientific, 31985-062) to a final volume of 950 µl in tube A. In tube B, 1 µg of DNA per
356 ml of media was mixed with pre-warmed Opti-MEM to a final volume of 950 µl. Then,
357 the contents of tube A and B were mixed, vortexed for 1 min and incubated at room
358 temperature for 15 min. Thereafter, the transfection mixture was added to the cell
359 suspension. 24h after transfection, EX-CELL 293 Serum-Free Medium (Sigma Aldrich,
360 14571C) was added to a final concentration of 20%. The transfected cells were grown
361 for 120h and the supernatants, containing the secreted lectin-mIgG2a fusion proteins,
362 harvested by centrifugation at 250g for 10 min.

363

364 Purification of the mouse lectin-mIgG2a fusion proteins was performed using Protein
365 A agarose resin (Gold Biotechnology, P-400-5). The protein A beads were pelleted at
366 150g for 5 min and washed once with 1x binding buffer (0.02 M Sodium Phosphate,
367 0.02% sodium azide, pH=7.0), before resuspending in 1x binding buffer. Immediately
368 preceding purification, aggregates were pelleted from the cell culture supernatant by
369 centrifugation for 10 min at 3000g. 10x binding buffer was added to the cell culture
370 supernatant to a final concentration of 1x as well as 4 µl of protein A beads per ml of
371 cell culture supernatant. The bead/ supernatant mixture was incubated overnight at 4
372 °C. The next morning, beads were collected by centrifugation for 5 min at 150g,
373 washed twice with 20 and 10 bead volumes of 1x binding buffer, the bead pellets
374 transferred to a 1ml spin column (G-Biosciences, 786-811) and washed once more

375 with 1 bead volume of 1x binding buffer. Excess buffer was removed by centrifugation
376 at 100g for 5 sec. Lectin-mIgG2a fusion proteins were eluted from the protein A beads
377 by resuspending the beads in 1 bead volume of Elution buffer (100mM Glycine-HCl,
378 pH=2-3, 0.02% sodium azide). After 30 sec of incubation the elution buffer was
379 collected into a 2 ml Eppendorf tube, containing Neutralization buffer (1M Tris, pH=9.0,
380 0.02% sodium azide) by centrifugation at 100g for 15 sec. Elution was performed for
381 a total of 3 times. The 3 eluted fractions were pooled and the protein concentrations
382 measured with the Pierce™ BCA Protein Assay Kit (ThermoFisher Scientific, 23225)
383 using the Pierce™ Bovine Gamma Globulin Standard (ThermoFisher Scientific,
384 23212). To confirm the purity of the eluted lectin-IgG fusion proteins, we performed an
385 SDS-PAGE, followed by a Coomassie staining. Briefly, 1 µg of eluted lectin-IgG fusion
386 protein was mixed with Sample Buffer, Laemmli 2x Concentrate (Sigma-Aldrich,
387 S3401) and heated to 95°C for 5 minutes. Thereafter, the samples were loaded onto
388 NuPage™ 4-12% Bis-Tris gels (ThermoFisher Scientific, NP0321BOX) and run in 1x
389 MOPS buffer at 140V for 45 minutes. The gel was subsequently stained with
390 InstantBlue™ Safe Coomassie Stain (Sigma-Aldrich, ISB1L) for 1h and de-stained
391 with distilled water. The gel picture was acquired with the ChemiDoc MP Imaging
392 System (BioRad) in the Coomassie setting.

393

394 **Recombinant expression of SARS-CoV-2 Spike protein and the receptor binding** 395 **domain (RBD).**

396 Recombinant protein expression was performed by transient transfection of HEK293-
397 6E cells, licensed from National Research Council (NRC) of Canada, as previously
398 described (Durocher et al., 2002; Lobner et al., 2017). Briefly, HEK293-6E cells were
399 cultivated in FreeStyle F17 expression medium (Thermo Fisher Scientific, A1383502)

400 supplemented with 0.1% (v/v) Pluronic F-68 (Thermo Fisher Scientific, 24040032) and
401 4 mM L-glutamine (Thermo Fisher Scientific, 25030081) in shaking flasks at 37°C, 8%
402 CO₂, 80% humidity and 130 rpm in a Climo-Shaker ISF1-XC (Adolf Kühner AG). The
403 pCAGGS vector constructs, containing either the sequence of the SARS-CoV-2 RBD
404 (residues R319-F541) or the complete luminal domain of the Spike protein (modified
405 by removing all arginine (R) residues from the polybasic furin cleavage site RRAR and
406 introduction of the stabilizing point mutations K986P and V987P) were kindly provided
407 by Florian Krammer, Icahn School of Medicine at Mount Sinai (NY, United States)
408 (Amanat et al., 2020; Stadlbauer et al., 2020). High quality plasmid preparations for
409 transfection were kindly provided by Rainer Hahn and Gerald Striedner (University of
410 Natural Resources and Life Sciences, Vienna, Austria). Transient transfection of the
411 cells was performed at a cell density of approximately 1.7×10^6 cells/mL culture volume
412 using a total of 1 µg of plasmid DNA and 2 µg of linear 40-kDa PEI (Polysciences,
413 24765-1) per mL culture volume. 48 h and 96 h after transfection, cells were
414 supplemented with 0.5% (w/v) tryptone N1 (Organotechnie 19553) and 0.25% (w/v)
415 D(+)-glucose (Carl Roth X997.1). Soluble proteins were harvested after 120-144 h by
416 centrifugation (10 000 g, 15 min, 4°C).

417

418 **SARS-CoV-2 Spike mutation frequency data.**

419 Annotated SARS-CoV-2 Spike mutations were extracted from the virus repository
420 nextstrain (<https://nextstrain.org/>); data are from sequences deposited until March
421 14th, 2021. The sites of N and S/T of all 22 *N*-glycan sequons (N-X-S/T) were
422 extracted, statistically compared using two-tailed Student's t-test and plotted with
423 GraphPad Prism.

424

425 **Purification of recombinant trimeric Spike protein and monomeric RBD of**
426 **SARS-CoV-2.**

427 For purification, the supernatants were filtered through 0.45 µm membrane filters
428 (Merck Millipore HAWP04700), concentrated and diafiltrated against 20 mM
429 phosphate buffer containing 500 mM NaCl and 20 mM imidazole (pH 7.4) using a
430 Labscale TFF system equipped with a 5 kDa cut-off Pellicon™ XL device (Merck
431 Millipore, PXC005C50). His-tagged trimer Spike and monomeric RBD were captured
432 using a 5 mL HisTrap FF crude column (Cytiva, 17528601) connected to an ÄKTA
433 pure chromatography system (Cytiva). Bound proteins were eluted by applying a linear
434 gradient of 20 to 500 mM imidazole over 20 column volumes. Fractions containing the
435 protein of interest were pooled, concentrated using Vivaspin 20 Ultrafiltration Units
436 (Sartorius, VS2011) and dialyzed against PBS (pH 7.4) at 4°C overnight using a
437 SnakeSkin Dialysis Tubing (Thermo Fisher Scientific, 68100). The RBD was further
438 polished by size exclusion chromatography (SEC) using a HiLoad 16/600 Superdex
439 200 pg column (Cytiva, 28-9893-35) equilibrated with PBS (pH 7.4). Both purified
440 proteins were stored at -80°C until further use.

441

442 **Glycoproteomic analysis of Spike and RBD.**

443 Peptide mapping and glycoproteomic analysis of all samples were performed on in-
444 solution proteolytic digests of the respective proteins by LC-ESI-MS(/MS). In brief, the
445 pH of the samples was adjusted to pH 7.8 by the addition of 1 M HEPES, pH 7.8 to a
446 final concentration of 100 mM HEPES, pH 7.8. The samples were then chemically
447 reduced and S-alkylated using a final concentration of 10 mM dithiothreitol for 30 min
448 at 56°C and a final concentration of 20 mM iodoacetamide for 30 min at room-
449 temperature in the dark, respectively. To maximize protein sequence-coverage of the

450 analysis, proteins were digested with either Trypsin (Promega), a combination of
451 Trypsin and GluC (Promega) or Chymotrypsin (Roche). Eventually, all proteolytic
452 digests were acidified by addition of 10% formic acid to pH 2 and directly analyzed by
453 LC-ESI-MS(/MS) using an a capillary BioBasic C18 reversed-phase column (BioBasic-
454 18, 150 x 0.32 mm, 5 μ m, Thermo Scientific), installed in an Ultimate U3000 HPLC
455 system (Dionex), developing a linear gradient from 95% eluent A (80 mM ammonium
456 formate, pH 3.0, in HPLC-grade water) to 65% eluent B (80% acetonitrile in 80 mM
457 ammonium formate, pH 3.0) over 50 min, followed by a linear gradient from 65% to
458 99% eluent B over 15 min, at a constant flow rate of 6 μ L/min, coupled to a maXis 4G
459 Q-TOF instrument (Bruker Daltonics; equipped with the standard ESI source). For
460 (glyco)peptide detection and identification, the mass-spectrometer was operated in
461 positive ion DDA mode (i.e. switching to MS/MS mode for eluting peaks), recording
462 MS-scans in the m/z range from 150 to 2200 Th, with the 6 highest signals selected
463 for MS/MS fragmentation. Instrument calibration was performed using a commercial
464 ESI calibration mixture (Agilent). Site-specific profiling of protein glycosylation was
465 performed using the dedicated Q-TOF data-analysis software packages Data Analyst
466 (Bruker Daltonics) and Protein Scape (Bruker Daltonics), in conjunction with the
467 MS/MS search engine MASCOT (Matrix Sciences Ltd.) for automated peptide
468 identification.

469

470 **ELISA assays to detect lectin binding to Spike and RBD.**

471 Briefly, 50 μ l of full-length Spike-H6 (4 μ g/ml, purified from HEK, diluted in PBS), RBD-
472 H6 (2 μ g/ml, purified from HEK, diluted in PBS) or human recombinant soluble ACE2
473 (hrsACE2; 4 μ g/ml, purified from CHO, diluted in PBS, see (Monteil et al., 2020)) per
474 well were used to coat a clear flat-bottom MaxiSorp 96-well plate (Thermo Fisher

475 Scientific, 442404) for 2h at 37°C. Thereafter, the coating solution was discarded and
476 the plate was washed 3 times with 300 µl of wash buffer (1xTBS, 1mM CaCl₂, 2mM
477 MgCl₂, 0.25% Triton X-100 (Sigma-Aldrich, T8787)). Unspecific binding was blocked
478 with 300 µl of blocking buffer (1xTBS, 1% BSA Fraction V (Applichem, A1391,0100),
479 1mM CaCl₂, 2mM MgCl₂ and 0.1% Tween-20 (Sigma-Aldrich, P1379)) for 30 min at
480 37°C. After removal of the blocking solution, 50 µl of either the mouse lectin-mIgG2a
481 (10 µg/ml, diluted in blocking buffer), human CD209-hIgG1 (R&D Systems, 161-DC-
482 050), human CD299-hIgG1 (R&D Systems, 162-D2-050), human CLEC4G-hIgG1
483 (Acro Biosystems, CLG-H5250-50ug) (10 µg/ml, diluted in blocking buffer),
484 recombinant human ACE2-mIgG1 (2 µg/ml, diluted in blocking buffer, Sino Biological,
485 10108-H05H) or recombinant human ACE2-hIgG1 (2 µg/ml, diluted in blocking buffer,
486 Sino Biological, 10108-H02H) were added for 1h at room temperature. After washing
487 for 3 times, 100 µl of 0.2 µg/ml HRP-conjugated goat anti-Mouse IgG (H+L) (Thermo
488 Fisher Scientific, 31430) or goat anti-Human IgG (H+L) (Promega, W4031) antibodies
489 were added for 30 min at room temperature. Subsequently, plates were washed as
490 described above. To detect binding, 1 tablet of OPD substrate (Thermo Fisher
491 Scientific, 34006) was dissolved in 9 ml of deionized water and 1ml of 10x Pierce™
492 Stable Peroxide Substrate Buffer (Thermo Fisher, Scientific, 34062). 100 µl of OPD
493 substrate solution were added per well and incubated for 15 min at room temperature.
494 The reaction was stopped by adding 75 µl of 2.5M sulfuric acid and absorption was
495 read at 490 nm. Absorption was measured for each lectin-Fc fusion protein tested
496 against full-length Spike-H6, RBD-H6 or hrsACE2 and normalized against bovine
497 serum albumin coated control wells.

498

499 **Protein denaturation and removal of N-glycans.**

500 To denature the full-length Spike-H6, 10 mM DTT was added to 40 µg/ml of protein.
501 The samples were incubated at 85°C for 10 min. Thereafter, the denatured proteins
502 were diluted to 4 µg/ml with PBS and a clear flat-bottom Maxisorp 96-well plate was
503 coated with 50 µl per well for 2h at 37°C. To remove the *N*-glycans from the full-length
504 Spike-H6, 0.2 µg protein were denatured as above and adjusted to a final
505 concentration of 1x Glycobuffer 2 containing 125U PNGase F per µg (NEB, P0704S)
506 in 50 µl. After incubation for 2h at 37°C, the reaction was stopped by heat-inactivation
507 for 10 min at 75°C. Spike proteins were then diluted to 4 µg/ml with PBS and a clear
508 flat-bottom Maxisorp 96-well plate was coated with 50 µl per well for 2h at 37°C. ELISA
509 protocols were performed as described above. To confirm the de-glycosylation of
510 Spike proteins, 0.5 µg were loaded on an SDS-PAGE gel followed by a Coomassie
511 staining.

512

513 **Surface plasmon resonance (SPR) measurements.**

514 A commercial SPR (BIAcore X, GE Healthcare, USA) was used to study the kinetics
515 of binding and dissociation of lectin-Fc dimers to the trimeric full-length Spike in real
516 time. Spike-H6 was immobilized on a Sensor Chip NTA (Cytiva, BR100034) via its
517 His6-tag after washing the chip for at least 3 minutes with 350 mM EDTA and activation
518 with a 1 min injection of 0.5 mM NiCl₂. 50 nM Spike were injected multiple times to
519 generate a stable surface. For the determination of kinetic and equilibrium constants,
520 the lectin samples (murine Clec4g, murine CD209c, human CLEC4G, human CD209)
521 were injected at different concentrations (10 to 500 nM). As the binding of the lectins
522 is Ca²⁺ dependent, lectins were removed from the surface by washing with degassed
523 calcium free buffer (TBS, 0.1% Tween-20, pH = 7.4). The resonance angle was
524 recorded at a 1 Hz sampling rate in both flow cells and expressed in resonance units

525 (1 RU = 0.0001°). The resulting experimental binding curves were fitted to the “bivalent
526 analyte model”, assuming a two-step binding of the lectins to immobilized Spike. All
527 evaluations were done using the BIAevaluation 3.2 software (BIAcore, GE Healthcare,
528 USA).

529

530 **Single molecule force spectroscopy (SMFS) measurements.**

531 For single molecule force spectroscopy a maleimide-Poly(ethylene glycol) (PEG)
532 linker was attached to 3-aminopropyltriethoxysilane (APTES)-coated atomic force
533 microscopy (AFM) cantilevers by incubating the cantilevers for 2h in 500 µL of
534 chloroform containing 1 mg of maleimide-PEG-N-hydroxysuccinimide (NHS)
535 (Polypure, 21138-2790) and 30 µl of triethylamine. After 3 times washing with
536 chloroform and drying with nitrogen gas, the cantilevers were immersed for 2h in a
537 mixture of 100 µL of 2 mM thiol-trisNTA, 2 µL of 100 mM EDTA (pH 7.5), 5 µL of 1 M
538 HEPES (pH 7.5), 2 µl of 100 mM tris(carboxyethyl)phosphine (TCEP) hydrochloride,
539 and 2.5 µL of 1 M HEPES (pH 9.6) buffer, and subsequently washed with HEPES-
540 buffered saline (HBS). Thereafter, the cantilevers were incubated for 4h in a mixture
541 of 4 µL of 5 mM NiCl₂ and 100 µL of 0.2 µM His-tagged Spike trimers. After washing
542 with HBS, the cantilevers were stored in HBS at 4°C (Oh et al., 2016). For the coupling
543 of lectins to surfaces, a maleimide-PEG linker was attached to an APTES-coated
544 silicon nitride surface. First, 2 µl of 100 mM TCEP, 2 µl of 1M HEPES (pH 9.6), 5 µl of
545 1M HEPES (pH 7.5), and 2 µl of 100 mM EDTA were added to 100 µl of 200 µg/ml
546 Protein A-Cys (pro-1992-b, Prospec, NJ, USA) in PBS. The surfaces were incubated
547 in this solution for 2h and subsequently washed with PBS and 0.02 M sodium
548 phosphate containing 0.02% sodium azide, pH=7.0. Finally, 100 µl of 200 µg/ml lectin-
549 Fc fusion proteins were added to the surfaces overnight.

550

551 Force distance measurements were performed at room temperature (~25 °C) with 0.01
552 N/m nominal spring constants (MSCT, Bruker) in TBS buffer containing 1 mM CaCl₂
553 and 0.1 % TWEEN-20. Spring constants of AFM cantilevers were determined by
554 measuring the thermally-driven mean-square bending of the cantilever using the
555 equipartition theorem in an ambient environment. The deflection sensitivity was
556 calculated from the slope of the force-distance curves recorded on a bare silicon
557 substrate. Determined spring constants ranged from 0.008 to 0.015 N/m. Force-
558 distance curves were acquired by recording at least 1000 curves with vertical sweep
559 rates between 0.5 and 10 Hz at a z-range of typically 500 – 1000 nm (resulting in
560 loading rates from 10 to 10,000 pN/s), using a commercial AFM (5500, Agilent
561 Technologies, USA). The relationship between experimentally measured unbinding
562 forces and parameters from the interaction potential were described by the kinetic
563 models of Bell (Bell, 1978) and Evans and Ritchie (Evans and Ritchie, 1997). In
564 addition, multiple parallel bond formation was calculated by the Williams model
565 (Williams, 2003) from the parameters derived from single bond analysis. The binding
566 probability was calculated from the number of force experiments displaying unbinding
567 events over the total number of force experiments.

568

569 The probability density function (PDF) of unbinding force was constructed from
570 unbinding events at the same pulling speed. For each unbinding force value, a
571 Gaussian unitary area was computed with its center representing the unbinding force
572 and the width (standard deviation) reflecting its measuring uncertainty (square root of
573 the variance of the noise in the force curve). All Gaussian areas from one experimental
574 setting were accordingly summed up and normalized with its binding activity to yield

575 the experimental PDF of unbinding force. PDFs are equivalents of continuous
576 histograms as shown in Fig. 3C.

577

578 **High-speed AFM (hsAFM) and data analysis.**

579 Purified SARS-CoV-2 trimeric Spike glycoproteins, murine Clec4g and CD209c and
580 hCLEC4g and hCD209 were diluted to 20 µg/ml with imaging buffer (20mM HEPES,
581 1mM CaCl₂, pH 7.4) and 1.5 µl of the protein solution was applied onto freshly cleaved
582 mica discs with diameters of 1.5 mm. After 3 minutes, the surface was rinsed with
583 ~15µL imaging buffer (without drying) and the sample was mounted into the imaging
584 chamber of the hsAFM (custom-built, RIBM, Japan). Movies were captured in imaging
585 buffer containing 3µg/ml of either Clec4g, CD209c, hCLEC4G or hCD209. An ultra-
586 short cantilever (USC-F1.2-k0.15 nominal spring constant 0.15 N/m, Nanoworld,
587 Switzerland) was used and areas of 100x100nm containing single molecules were
588 selected to capture the hsAFM movies at a scan rate of ~150-300 ms per frame.
589 During the acquisition of the movies, the amplitude was kept constant and set to 90-
590 85% of the free amplitude (typically ~3 nm). Data analysis was performed using the
591 Gwyddion 2.55 software. Images were processed to remove background and transient
592 noise. For volume measurements, a height threshold mask was applied over the
593 protein structures with a minimum height of 0.25 – 0.35 nm to avoid excessive
594 background noise in the masked area. The numbers of lectin molecules bound to the
595 Spike trimers was calculated based on the measured mean volumes of the full-length
596 Spike, the lectins, and the Spike-lectin complexes, averaged over the recorded time-
597 periods.

598

599 **AFM measured Spike binding to Vero E6 cells.**

600 Vero E6 cells were grown on culture dishes using DMEM containing 10% FBS, 500
601 units/mL penicillin and 100 µg/mL streptomycin, at 37°C with 5% CO₂. For AFM
602 measurements, the cell density was adjusted to about 10-30% confluency. Before the
603 measurements, the growth medium was exchanged to a physiological HEPES buffer
604 containing 140 mM NaCl, 5 mM KCl, 1 mM MgCl₂, 1 mM CaCl₂, and 10 mM HEPES
605 (pH 7.4). Lectins were added at the indicated concentrations. Using a full-length Spike
606 trimer anchored to an AFM cantilever (described above), force-distance curves were
607 recorded at room temperature on living cells with the assistance of a CCD camera for
608 localization of the cantilever tip on selected cells. The sweep range was fixed at 3000
609 nm and the sweep rate was set at 1 Hz. For each cell, at least 100 force-distance
610 cycles with 2000 data points per cycle and a typical force limit of about 30 pN were
611 recorded.

612

613 **Glycan array analyses.**

614 The glycan microarrays were analyzed by Asparia Glycomics (San Sebastian, Spain)
615 and prepared as described previously (Brzezicka et al., 2015). Briefly, 50 µM ligand
616 solutions (1.25 nL, 5 drops, 250 pL drop volume) in sodium phosphate buffer (300 mM,
617 0.005% Tween-20, pH=8.4) were spatially arrayed employing a robotic non-contact
618 piezoelectric spotter (SciFLEXARRAYER S11, Scienion) onto N-hydroxysuccinimide
619 (NHS) activated glass slides (Nexterion H, Schott AG). After printing, the slides were
620 placed in a 75 % humidity chamber for 18 hours at 25°C. The remaining NHS groups
621 were quenched with 50 mM solution of ethanolamine in sodium borate buffer (50 mM,
622 pH=9.0) for 1h. The slides were washed with PBST (PBS/0.05% Tween-20), PBS and
623 water, then dried in a slide spinner and stored at -20°C until use.

624

625 Glycan microarrays were compartmentalized using Proplate® 8 wells microarray
626 gaskets, generating 7 independent subarrays per slide. Fusion proteins were diluted
627 at a final concentration (10 µg/mL) in binding buffer (25mM Tris, 150 mM NaCl, 4 mM
628 CaCl₂ and 0.005% Tween 20 containing 0.5 % bovine serum albumin). Lectins were
629 applied to the microarrays and incubated at 4°C overnight with gentle shaking. The
630 solutions were removed and arrays washed with binding buffer without BSA at room
631 temperature. Interactions were visualized by the incubation of tetramethylrhodamine
632 (TRITC) labelled secondary goat anti-mouse IgG antibodies (Fc specific; 1:1000
633 dilution in binding buffer ; Life Technologies) and goat anti-Human IgG (Fc specific)-
634 Cy3 (1:1000 dilution in binding buffer; Merck). Finally, slides were washed with binding
635 buffer without BSA, dried in a slide spinner and scanned. Fluorescence was analyzed
636 using an Agilent G265BA microarray scanner (Agilent Technologies). The
637 quantification of fluorescence was done using ProScanArray Express software (Perkin
638 Elmer) employing an adaptive circle quantification method from 50 µm (minimum spot
639 diameter) to 300 µm (maximum spot diameter). Average RFU (relative fluorescence
640 unit) values with local background subtraction of four spots and standard deviation of
641 the mean were recorded using Microsoft Excel and GraphPad Prism.

642

643 **Structural modelling.**

644 Structural models of the SARS-CoV-2 Spike protein were based on the model of the
645 fully glycosylated Spike-hACE2 complex. Experimental structures deposited in the
646 protein databank (PDB) were used to model the complex that is formed by the binding
647 of SARS-CoV-2 Spike and ACE2 (Walls et al., 2020; Yan et al., 2020). RBD domain
648 in complex with ACE2 was superimposed with Spike with one open RBD domain
649 (PDB: 6VYB) and SWISS-MODEL was used to model missing residues in Spike

650 (Waterhouse et al., 2018) (GenBank QHD43416.1). Glycan structures in agreement
651 with the assignments of the current work were added using the methodology outlined
652 by Turupcu et al (Turupcu and Oostenbrink, 2017). The full model is available at the
653 MolSSI / BioExcel COVID-19 Molecular Structure and Therapeutics Hub
654 ([https://covid.molssi.org//models/#spike-protein-in-complex-with-human-ace2-spike-](https://covid.molssi.org//models/#spike-protein-in-complex-with-human-ace2-spike-spike-binding)
655 [spike-binding](https://covid.molssi.org//models/#spike-protein-in-complex-with-human-ace2-spike-spike-binding)). For hCLEC4G a homology model of residues 118 – 293 was
656 constructed using Swiss-Model (Waterhouse et al., 2018) using residues 4 – 180 of
657 chain A of the crystal structure of the carbohydrate recognition domain of DC-SIGNR
658 (CD299) (PDB-code 1sl6, (Guo et al., 2004)). This fragment shows a sequence identity
659 of 36% with hCLEC4G, and the resulting model showed an overall QMEAN value of -
660 2.68. For mClec4g, the model consisted of residues 118 – 294, with a sequence
661 identity of 38 % to the same template model. The resulting QMEAN value was -2.88.
662 A calcium ion and the bound Lewis x oligosaccharide of the template were taken over
663 into the model, indicating the location of the carbohydrate binding site. For hCD209,
664 the crystal structure of the carbohydrate recognition domain of CD209 (DC-SIGN)
665 complexed with Man4 (PDB code 1sl4, (Guo et al., 2004)) was used. To identify
666 binding sites of hCLEC4G and hCD209 to the Spike-hACE2 complex, a superposition
667 of the bound carbohydrates with the glycans on Spike was performed. For hCLEC4G,
668 we used the complex glycans at N343 of the third monomer of Spike, with the receptor
669 binding domain in an ‘up’ position, while N343 glycans on monomer 1 and 2 were
670 modelled with the receptor binding domain in a ‘down’ position. For hCD209 we used
671 the high-mannose glycan at position N234 in monomer 1-3 of Spike, respectively.
672 These glycan structures were chosen in accordance with the full-length Spike
673 glycoproteome.
674

675 **SARS-CoV-2 infections.**

676 Vero E6 cells were seeded in 48-well plates (5×10^4 cells per well) (Sarstedt, 83.3923)
677 in DMEM containing 10% FBS. 24 hours post-seeding, different concentrations of
678 lectins were mixed with 10^3 PFU of virus (1:1) to a final volume of 100 μ l per well in
679 DMEM (resulting in a final concentration of 5% FBS). After incubation for 30 min at
680 37°C, Vero E6 were infected either with mixes containing lectins/SARS-CoV-2, SARS-
681 CoV-2 alone, or mock infected. 15 hours post-infection, supernatants were removed,
682 cells were washed 3 times with PBS and then lysed using Trizol Reagent (Thermo
683 Fisher Scientific, 15596026). The qRT-PCR for the detection of viral RNA was
684 performed as previously described (Monteil et al., 2020). Briefly, RNA was extracted
685 using the Direct-zol RNA MiniPrep kit (Zymo Research, R2051). The qRT-PCR was
686 performed for the SARS-CoV-2 E gene and RNase P was used as an endogenous
687 gene control to normalize viral RNA levels to the cell number. Lectins were
688 independently tested for cellular toxicity in an ATP-dependent assay (Cell-Titer Glo,
689 Promega) and cells found to exhibit >80% viability up to a concentration of 200 μ g/ml
690 (data not shown).

691

692 The following PCR Primers were used:

693 SARS-CoV2 E-gene:

694 Forward primer: 5'-ACAGGTACGTTAATAGTTAATAGCGT-3'

695 Reverse primer: 5'-ATATTGCAGCAGTACGCACACA-3'

696 Probe: FAM-ACACTAGCCATCCTTACTGCGCTTCG-QSY

697

698 RNase P:

699 Forward primer: 5'-AGATTTGGACCTGCGAGCG-3'

700 Reverse primer 5'-GAGCGGCTGTCTCCACAAGT-3'

701 Probe: FAM-TTCTGACCTGAAGGCTCTGCGCG-MGB

702

703

704 **Acknowledgements:** We thank all members of the Penninger laboratory for helpful
705 discussions and technical support. Moreover, we thank all members of the Molecular
706 Biology Service and the VBCF Protein Technologies Facility. We thank Florian
707 Krammer (Icahn School of Medicine at Mount Sinai, NY, United States) for providing
708 the constructs used for production of recombinant Spike and RBD. Purified Spike and
709 RBD as well as transfection-grade pCAGGS plasmids were obtained from the reagent
710 repository of the BOKU COVID-19 Initiative. The authors thank Daniel Maresch
711 (BOKU Core Facility Mass Spectrometry) for assistance with glycan analysis. Fig. 1A,
712 3A and S1A created with BioRender.com. J.M.P. and the research leading to these
713 results has received funding from the T. von Zastrow foundation, the FWF Wittgenstein
714 award (Z 271-B19), the Austrian Academy of Sciences, the Innovative Medicines
715 Initiative 2 Joint Undertaking (JU) under grant agreement No 101005026, and the
716 Canada 150 Research Chairs Program F18-01336 as well as the Canadian Institutes
717 of Health Research COVID-19 grants F20-02343 and F20-02015. D.H. is supported
718 by the T. von Zastrow foundation, S.M. is funded by the European Union's Horizon
719 2020 research and innovation programme under the Marie Skłodowska-Curie grant
720 agreement No 841319. We further acknowledge financial support from the Austrian
721 National Foundation for Research, Technology, and Development and Research
722 Department of the State of Upper Austria (Y.J.O), from the FWF projects V584 (Y.J.O),
723 P31599 (R.Z.), I3173 (P.H., L.H.), the WWTF grant LS19-029 (P.H, D.C.) and grant
724 COV20-015 (C.O.), the ÖAW fellowship STIP13202002 (L.H.), and the European

725 Union's Horizon research and innovation programme (H2020-MSCA-ITN-2016) under
726 the Marie Skłodowska-Curie grant agreement No. 721874 (P.H., D.C.). A.M. and V.M.
727 have received funding from the Innovative Medicines Initiative 2 JU under grant
728 agreement no. 101005026. JU receives support from the European Union's Horizon
729 2020 research and innovation programme and EFPIA.

730

731 **Author contributions:** D.H., S.M. and J.M.P. conceived and designed the study;
732 Y.J.O. and P.H. conceived and coordinated the SPR and AFM studies; Y.J.O.
733 performed the lectin force spectroscopy measurements and data analysis; R.Z.
734 performed the binding activity measurements and data analysis; D.C. performed the
735 high-speed AFM measurements and data analysis; L.H. performed the SPR
736 measurements and data analysis; V.M. and A.M. designed, performed and analyzed
737 the SARS-CoV-2 infection experiments; E.L. and L.M. set-up and performed the
738 purification of the Spike and RBD; C.G.G., F.A. and J.S. designed, performed and
739 analyzed the glycosylation of the Spike and RBD; D.H., G.W., M.N., A.C. and M.T.
740 designed, set-up and purified the lectin-Fc proteins; D.H., A.H. and S.M. performed all
741 ELISA experiments; C.O. performed the modelling; Y.J.O., R.Z., D.C. and L.H. wrote
742 the original SPR and AFM part of this manuscript with guidance and edits from P.H.;
743 D.H., S.M. and J.M.P. wrote the manuscript. All authors read and reviewed of the
744 manuscript.

745

746 **Conflict of interest:** A patent is being prepared to use CLEC4G as potential therapy
747 for COVID-19. J.M.P. is shareholder and board member of Apeiron Biologics that is
748 developing soluble ACE2 for COVID-19 therapy.

749

750 **References:**

- 751 Amanat, F., Stadlbauer, D., Strohmeier, S., Nguyen, T.H.O., Chromikova, V.,
752 McMahon, M., Jiang, K., Asthagiri Arunkumar, G., Jurczynszak, D., Polanco, J., *et al.*
753 (2020). A serological assay to detect SARS-CoV-2 seroconversion in humans.
754 medRxiv.
- 755 Appelmelk, B.J., van Die, I., van Vliet, S.J., Vandenbroucke-Grauls, C.M.,
756 Geijtenbeek, T.B., and van Kooyk, Y. (2003). Cutting edge: carbohydrate profiling
757 identifies new pathogens that interact with dendritic cell-specific ICAM-3-grabbing
758 nonintegrin on dendritic cells. *J Immunol* *170*, 1635-1639.
- 759 Bell, G.I. (1978). Models for the specific adhesion of cells to cells. *Science* *200*, 618-
760 627.
- 761 Brzezicka, K., Echeverria, B., Serna, S., van Diepen, A., Hokke, C.H., and Reichardt,
762 N.C. (2015). Synthesis and microarray-assisted binding studies of core xylose and
763 fucose containing N-glycans. *ACS Chem Biol* *10*, 1290-1302.
- 764 Dominguez-Soto, A., Aragoneses-Fenoll, L., Gomez-Aguado, F., Corcuera, M.T.,
765 Claria, J., Garcia-Monzon, C., Bustos, M., and Corbi, A.L. (2009). The pathogen
766 receptor liver and lymph node sinusoidal endothelial cell C-type lectin is expressed in
767 human Kupffer cells and regulated by PU.1. *Hepatology* *49*, 287-296.
- 768 Dominguez-Soto, A., Aragoneses-Fenoll, L., Martin-Gayo, E., Martinez-Prats, L.,
769 Colmenares, M., Naranjo-Gomez, M., Borrás, F.E., Munoz, P., Zubiaur, M., Toribio,
770 M.L., *et al.* (2007). The DC-SIGN-related lectin LSECtin mediates antigen capture
771 and pathogen binding by human myeloid cells. *Blood* *109*, 5337-5345.
- 772 Durocher, Y., Perret, S., and Kamen, A. (2002). High-level and high-throughput
773 recombinant protein production by transient transfection of suspension-growing
774 human 293-EBNA1 cells. *Nucleic Acids Res* *30*, E9.
- 775 Evans, E., and Ritchie, K. (1997). Dynamic strength of molecular adhesion bonds.
776 *Biophys J* *72*, 1541-1555.
- 777 Gao, C., Zeng, J., Jia, N., Stavenhagen, K., Matsumoto, Y., Zhang, H., Li, J., Hume,
778 A.J., Muhlberger, E., van Die, I., *et al.* (2020). SARS-CoV-2 Spike Protein Interacts
779 with Multiple Innate Immune Receptors. bioRxiv.
- 780 Garcia-Vallejo, J.J., and van Kooyk, Y. (2013). The physiological role of DC-SIGN: a
781 tale of mice and men. *Trends Immunol* *34*, 482-486.
- 782 Gramberg, T., Hofmann, H., Moller, P., Lalor, P.F., Marzi, A., Geier, M., Krumbiegel,
783 M., Winkler, T., Kirchhoff, F., Adams, D.H., *et al.* (2005). LSECtin interacts with
784 filovirus glycoproteins and the spike protein of SARS coronavirus. *Virology* *340*, 224-
785 236.
- 786 Guo, Y., Feinberg, H., Conroy, E., Mitchell, D.A., Alvarez, R., Blixt, O., Taylor, M.E.,
787 Weis, W.I., and Drickamer, K. (2004). Structural basis for distinct ligand-binding and
788 targeting properties of the receptors DC-SIGN and DC-SIGNR. *Nat Struct Mol Biol*
789 *11*, 591-598.
- 790 Hinterdorfer, P., Baumgartner, W., Gruber, H.J., Schilcher, K., and Schindler, H.
791 (1996). Detection and localization of individual antibody-antigen recognition events
792 by atomic force microscopy. *Proc Natl Acad Sci U S A* *93*, 3477-3481.

793 Hoffmann, M., Kleine-Weber, H., Schroeder, S., Kruger, N., Herrler, T., Erichsen, S.,
794 Schiergens, T.S., Herrler, G., Wu, N.H., Nitsche, A., *et al.* (2020). SARS-CoV-2 Cell
795 Entry Depends on ACE2 and TMPRSS2 and Is Blocked by a Clinically Proven
796 Protease Inhibitor. *Cell* *181*, 271-280 e278.

797 Ke, Z., Oton, J., Qu, K., Cortese, M., Zila, V., McKeane, L., Nakane, T., Zivanov, J.,
798 Neufeldt, C.J., Cerikan, B., *et al.* (2020). Structures and distributions of SARS-CoV-2
799 spike proteins on intact virions. *Nature*.

800 Knolle, P.A., and Wohlleber, D. (2016). Immunological functions of liver sinusoidal
801 endothelial cells. *Cell Mol Immunol* *13*, 347-353.

802 Kodera, N., Yamamoto, D., Ishikawa, R., and Ando, T. (2010). Video imaging of
803 walking myosin V by high-speed atomic force microscopy. *Nature* *468*, 72-76.

804 Li, Q., Wu, J., Nie, J., Zhang, L., Hao, H., Liu, S., Zhao, C., Zhang, Q., Liu, H., Nie,
805 L., *et al.* (2020). The Impact of Mutations in SARS-CoV-2 Spike on Viral Infectivity
806 and Antigenicity. *Cell*.

807 Liu, W., Tang, L., Zhang, G., Wei, H., Cui, Y., Guo, L., Gou, Z., Chen, X., Jiang, D.,
808 Zhu, Y., *et al.* (2004). Characterization of a novel C-type lectin-like gene, LSECtin:
809 demonstration of carbohydrate binding and expression in sinusoidal endothelial cells
810 of liver and lymph node. *J Biol Chem* *279*, 18748-18758.

811 Lobner, E., Humm, A.S., Goritzer, K., Mlynek, G., Puchinger, M.G., Hasenhindl, C.,
812 Ruker, F., Traxlmayr, M.W., Djinojic-Carugo, K., and Obinger, C. (2017). Fcab-
813 HER2 Interaction: a Menage a Trois. Lessons from X-Ray and Solution Studies.
814 *Structure* *25*, 878-889 e875.

815 Monteil, V., Kwon, H., Prado, P., Hagelkruys, A., Wimmer, R.A., Stahl, M., Leopoldi,
816 A., Garreta, E., Hurtado Del Pozo, C., Prosper, F., *et al.* (2020). Inhibition of SARS-
817 CoV-2 Infections in Engineered Human Tissues Using Clinical-Grade Soluble
818 Human ACE2. *Cell* *181*, 905-913 e907.

819 Oh, Y.J., Hubauer-Brenner, M., Gruber, H.J., Cui, Y., Traxler, L., Siligan, C., Park,
820 S., and Hinterdorfer, P. (2016). Curli mediate bacterial adhesion to fibronectin via
821 tensile multiple bonds. *Sci Rep* *6*, 33909.

822 Osorio, F., and Reis e Sousa, C. (2011). Myeloid C-type lectin receptors in pathogen
823 recognition and host defense. *Immunity* *34*, 651-664.

824 Pipirou, Z., Powlesland, A.S., Steffen, I., Pohlmann, S., Taylor, M.E., and Drickamer,
825 K. (2011). Mouse LSECtin as a model for a human Ebola virus receptor.
826 *Glycobiology* *21*, 806-812.

827 Powlesland, A.S., Fisch, T., Taylor, M.E., Smith, D.F., Tissot, B., Dell, A., Pohlmann,
828 S., and Drickamer, K. (2008). A novel mechanism for LSECtin binding to Ebola virus
829 surface glycoprotein through truncated glycans. *J Biol Chem* *283*, 593-602.

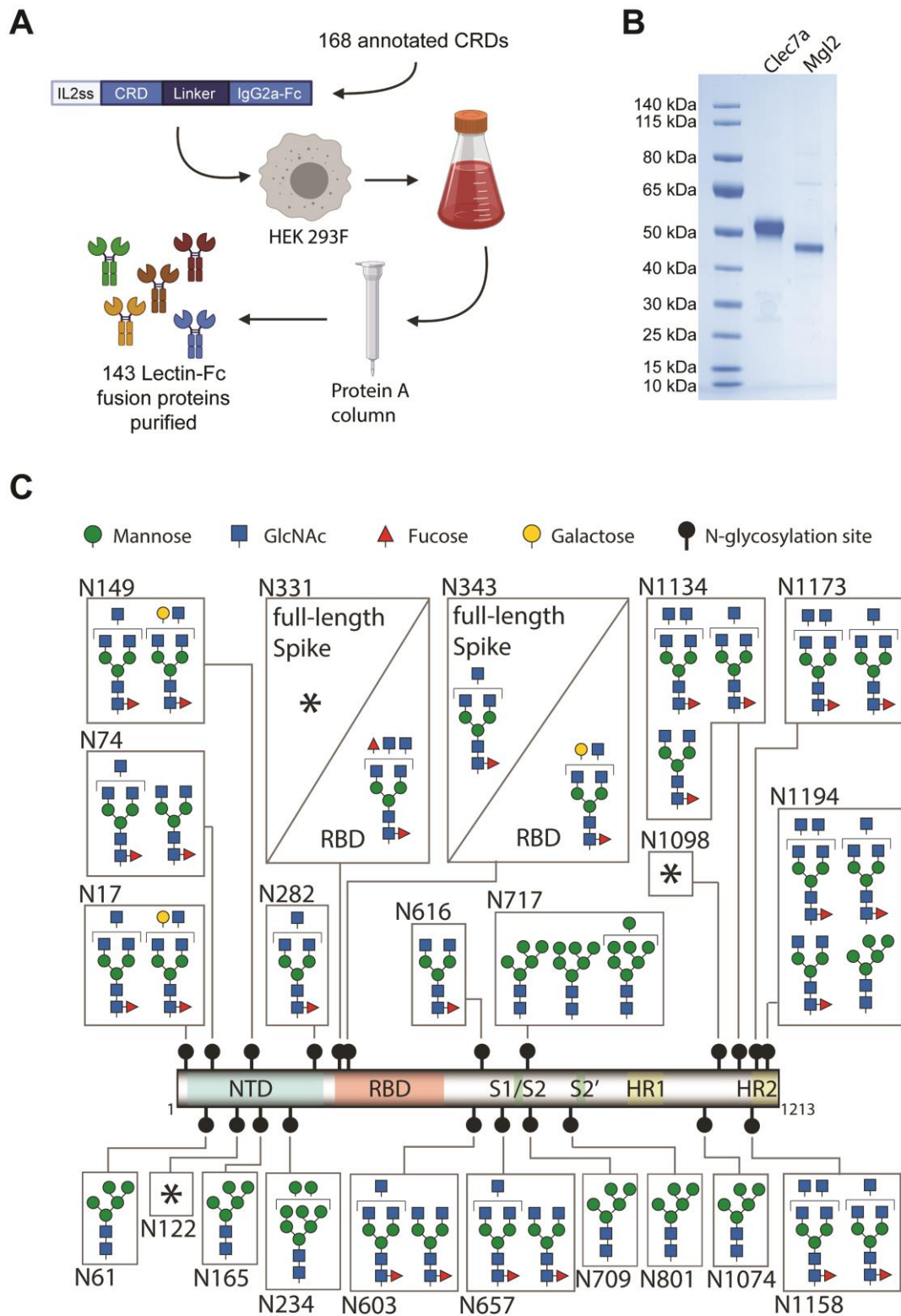
830 Preiner, J., Kodera, N., Tang, J., Ebner, A., Brameshuber, M., Blaas, D., Gelbmann,
831 N., Gruber, H.J., Ando, T., and Hinterdorfer, P. (2014). IgGs are made for walking on
832 bacterial and viral surfaces. *Nat Commun* *5*, 4394.

833 Rankl, C., Kienberger, F., Wildling, L., Wruss, J., Gruber, H.J., Blaas, D., and
834 Hinterdorfer, P. (2008). Multiple receptors involved in human rhinovirus attachment
835 to live cells. *Proc Natl Acad Sci U S A* *105*, 17778-17783.

836 Shang, J., Wan, Y., Luo, C., Ye, G., Geng, Q., Auerbach, A., and Li, F. (2020). Cell
837 entry mechanisms of SARS-CoV-2. *Proc Natl Acad Sci U S A* *117*, 11727-11734.
838 Stadlbauer, D., Amanat, F., Chromikova, V., Jiang, K., Strohmeier, S., Arunkumar,
839 G.A., Tan, J., Bhavsar, D., Capuano, C., Kirkpatrick, E., *et al.* (2020). SARS-CoV-2
840 Seroconversion in Humans: A Detailed Protocol for a Serological Assay, Antigen
841 Production, and Test Setup. *Curr Protoc Microbiol* *57*, e100.
842 Stanley, P., Taniguchi, N., and Aebi, M. (2015). N-Glycans. In *Essentials of*
843 *Glycobiology*, rd, A. Varki, R.D. Cummings, J.D. Esko, P. Stanley, G.W. Hart, M.
844 Aebi, A.G. Darvill, T. Kinoshita, N.H. Packer, *et al.*, eds. (Cold Spring Harbor (NY)),
845 pp. 99-111.
846 Thépaut, M., Luczkowiak, J., Vivès, C., Labiod, N., Bally, I., Lasala, F., Grimoire, Y.,
847 Fenel, D., Sattin, S., Thielens, N., *et al.* (2020). DC/L-SIGN recognition of spike
848 glycoprotein promotes SARS-CoV-2 trans-infection and can be inhibited by a
849 glycomimetic antagonist. *bioRxiv*.
850 Traxler, L., Rathner, P., Fahrner, M., Stadlbauer, M., Faschinger, F., Charnavets, T.,
851 Muller, N., Romanin, C., Hinterdorfer, P., and Gruber, H.J. (2017). Detailed Evidence
852 for an Unparalleled Interaction Mode between Calmodulin and Orai Proteins. *Angew*
853 *Chem Int Ed Engl* *56*, 15755-15759.
854 Turupcu, A., and Oostenbrink, C. (2017). Modeling of Oligosaccharides within
855 Glycoproteins from Free-Energy Landscapes. *J Chem Inf Model* *57*, 2222-2236.
856 Van Breedam, W., Pohlmann, S., Favoreel, H.W., de Groot, R.J., and Nauwynck,
857 H.J. (2014). Bitter-sweet symphony: glycan-lectin interactions in virus biology. *FEMS*
858 *Microbiol Rev* *38*, 598-632.
859 Walls, A.C., Park, Y.J., Tortorici, M.A., Wall, A., McGuire, A.T., and Veesler, D.
860 (2020). Structure, Function, and Antigenicity of the SARS-CoV-2 Spike Glycoprotein.
861 *Cell* *181*, 281-292 e286.
862 Watanabe, Y., Allen, J.D., Wrapp, D., McLellan, J.S., and Crispin, M. (2020a). Site-
863 specific glycan analysis of the SARS-CoV-2 spike. *Science* *369*, 330-333.
864 Watanabe, Y., Berndsen, Z.T., Raghvani, J., Seabright, G.E., Allen, J.D., Pybus,
865 O.G., McLellan, J.S., Wilson, I.A., Bowden, T.A., Ward, A.B., *et al.* (2020b).
866 Vulnerabilities in coronavirus glycan shields despite extensive glycosylation. *Nat*
867 *Commun* *11*, 2688.
868 Watanabe, Y., Bowden, T.A., Wilson, I.A., and Crispin, M. (2019). Exploitation of
869 glycosylation in enveloped virus pathobiology. *Biochim Biophys Acta Gen Subj* *1863*,
870 1480-1497.
871 Waterhouse, A., Bertoni, M., Bienert, S., Studer, G., Tauriello, G., Gumienny, R.,
872 Heer, F.T., de Beer, T.A.P., Rempfer, C., Bordoli, L., *et al.* (2018). SWISS-MODEL:
873 homology modelling of protein structures and complexes. *Nucleic Acids Res* *46*,
874 W296-W303.
875 Williams, P.M. (2003). Analytical descriptions of dynamic force spectroscopy:
876 behaviour of multiple connections. *Anal Chim Acta* *479*, 107-115.
877 Yan, R., Zhang, Y., Li, Y., Xia, L., Guo, Y., and Zhou, Q. (2020). Structural basis for
878 the recognition of SARS-CoV-2 by full-length human ACE2. *Science* *367*, 1444-
879 1448.

880 Zhu, R., Howorka, S., Proll, J., Kienberger, F., Preiner, J., Hesse, J., Ebner, A.,
881 Pastushenko, V.P., Gruber, H.J., and Hinterdorfer, P. (2010). Nanomechanical
882 recognition measurements of individual DNA molecules reveal epigenetic
883 methylation patterns. *Nat Nanotechnol* 5, 788-791.
884

Figure 1



885

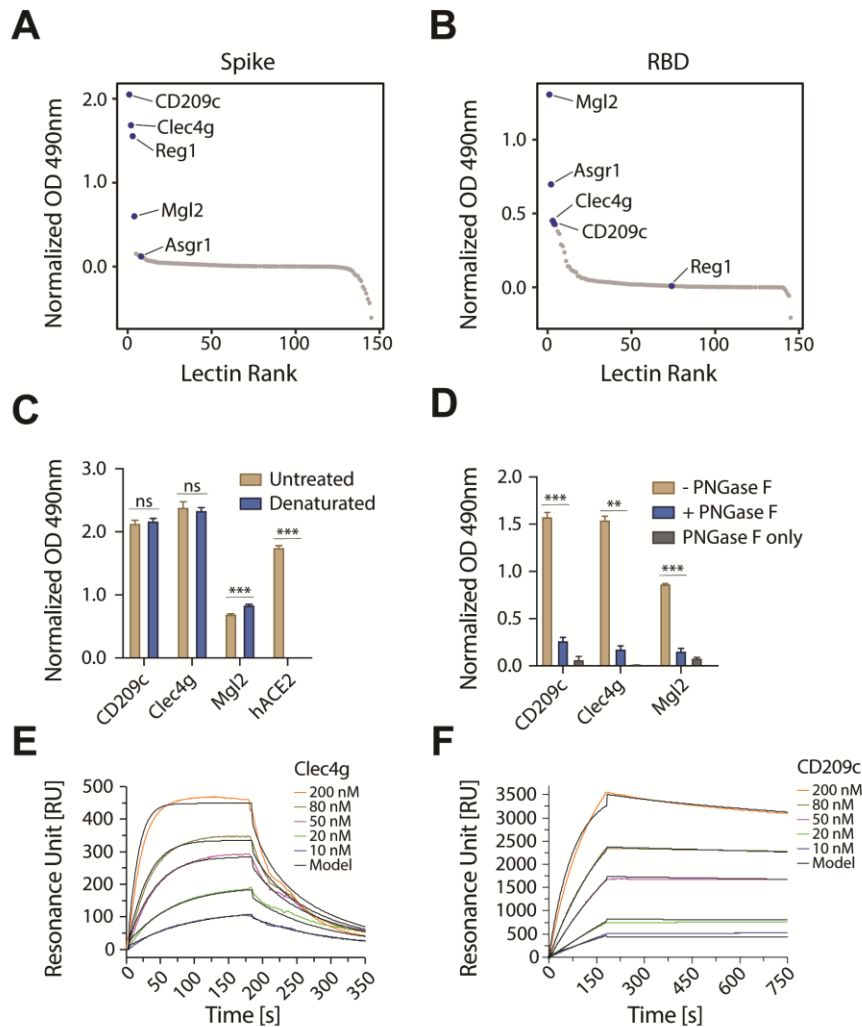
886

887

888 **Figure 1. Lectin library and SARS-CoV-2 Spike and RBD glycosylation.**

889 (A) Schematic overview of cloning, expression and purification of 143 carbohydrate
890 recognition domain (CRD) – mouse IgG2a-Fc fusion proteins, from 168 annotated
891 murine CRD containing proteins. The constructs were expressed in HEK293F cells
892 and secreted Fc-fusion proteins were purified using protein A columns. See table S1
893 for full list of expressed CRDs. (B) Exemplified SDS-PAGE of purified Clec7a and Mgl2
894 stained with Coomassie blue. (C) Glycosylation map of the SARS-CoV-2 Spike and
895 RBD. The most prominent glycan structures are represented for each site, with at least
896 15% relative abundance. * marks highly variable glycosylation sites in which no single
897 glycan structure accounted for >15% relative abundance. The different
898 monosaccharides are indicated using standardized nomenclature. NTD, n-terminal
899 domain; RBD, receptor binding domain; S1/S2 and S2', proteolytic cleavage sites;
900 HR1 and HR2, α -helical heptad repeat domains 1 and 2; GlcNAc, N-
901 acetylglucosamine.
902

Figure 2



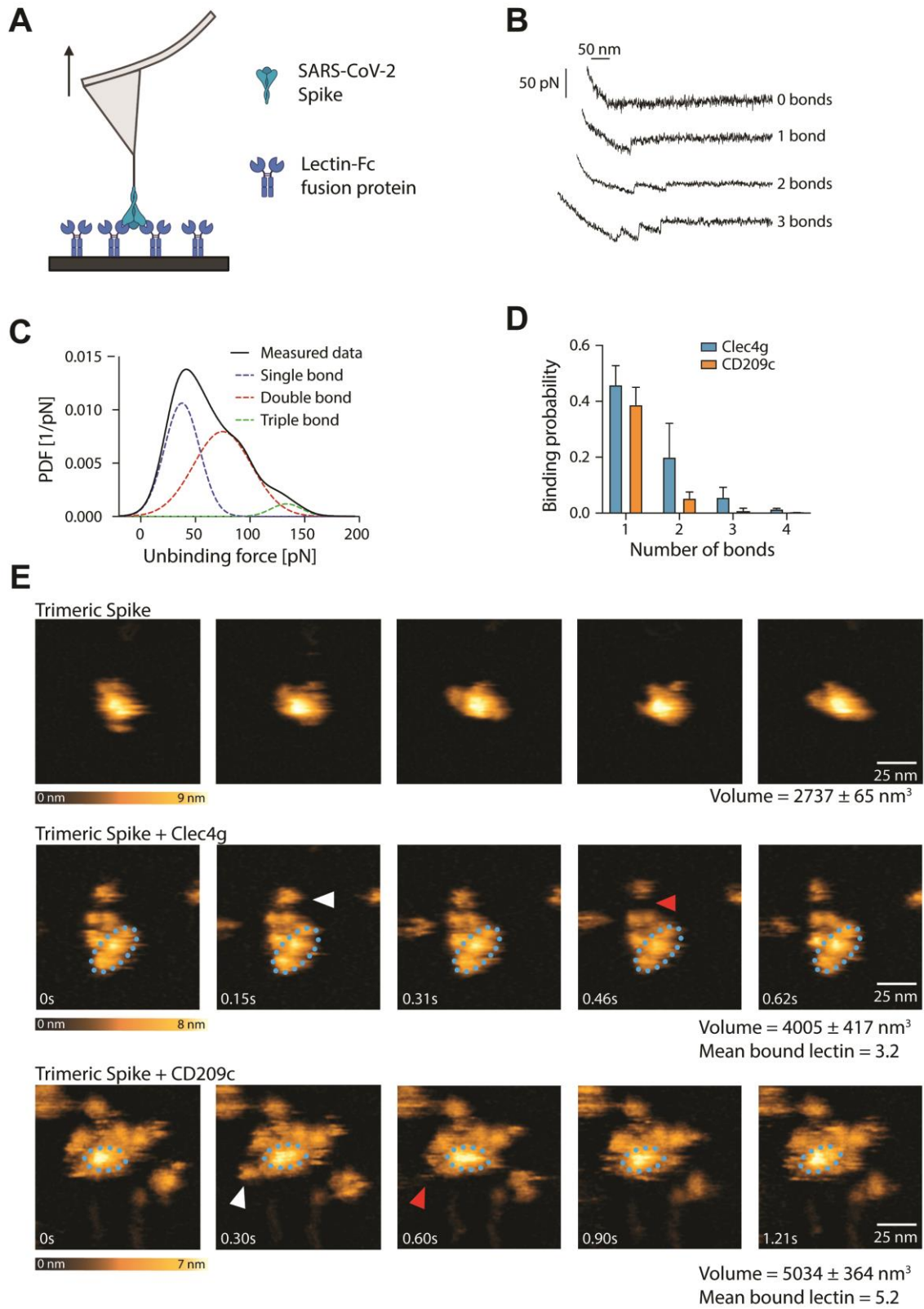
903

904 **Figure 2. Identification of lectins that bind to Spike and RBD of SARS-CoV-2.**

905 (A) and (B) ELISA screen of the lectin-Fc library against full-length trimeric SARS-
906 CoV-2 Spike (A) or monomeric RBD (B). Results are shown as mean OD values of 2
907 replicates normalized against a BSA control and ranked by value. Lectin-Fc fusion
908 proteins with a normalized OD > 0.5 in either (A) or (B) are indicated in both panels.
909 See table S2 for primary ELISA data. (C) Lectin-Fc and human ACE2-mIgG1 Fc-fusion
910 protein (hACE2) binding to untreated or heat-denatured full-length SARS-CoV-2 Spike
911 by ELISA. hACE2-mIgG1 was used as control for complete denaturation of Spike
912 protein. Results are shown as mean OD values \pm SD normalized to the BSA control

913 (N=3). **(D)** Lectin-Fc binding to full-length SARS-CoV-2 Spike with or without de-*N*-
914 glycosylation by PNGase F. “PNGase F only” denotes wells that were not coated with
915 the Spike protein. Results are shown as mean OD values \pm SD normalized to BSA
916 controls (N=3). **(E)** and **(F)** Surface plasmon resonance (SPR) analysis with
917 immobilized full-length trimeric Spike, probed with various concentrations of Clec4g-
918 Fc (E) and CD209c-Fc (F). See Table 1 for kinetics values. **(C)** t-test with Holm-Sidak
919 correction for multiple comparisons. **(D)** One-way ANOVA with Tukey’s multiple
920 comparisons; *P<0.05; **P<0.01; ***P<0.001; ns: not significant.
921

Figure 3



922

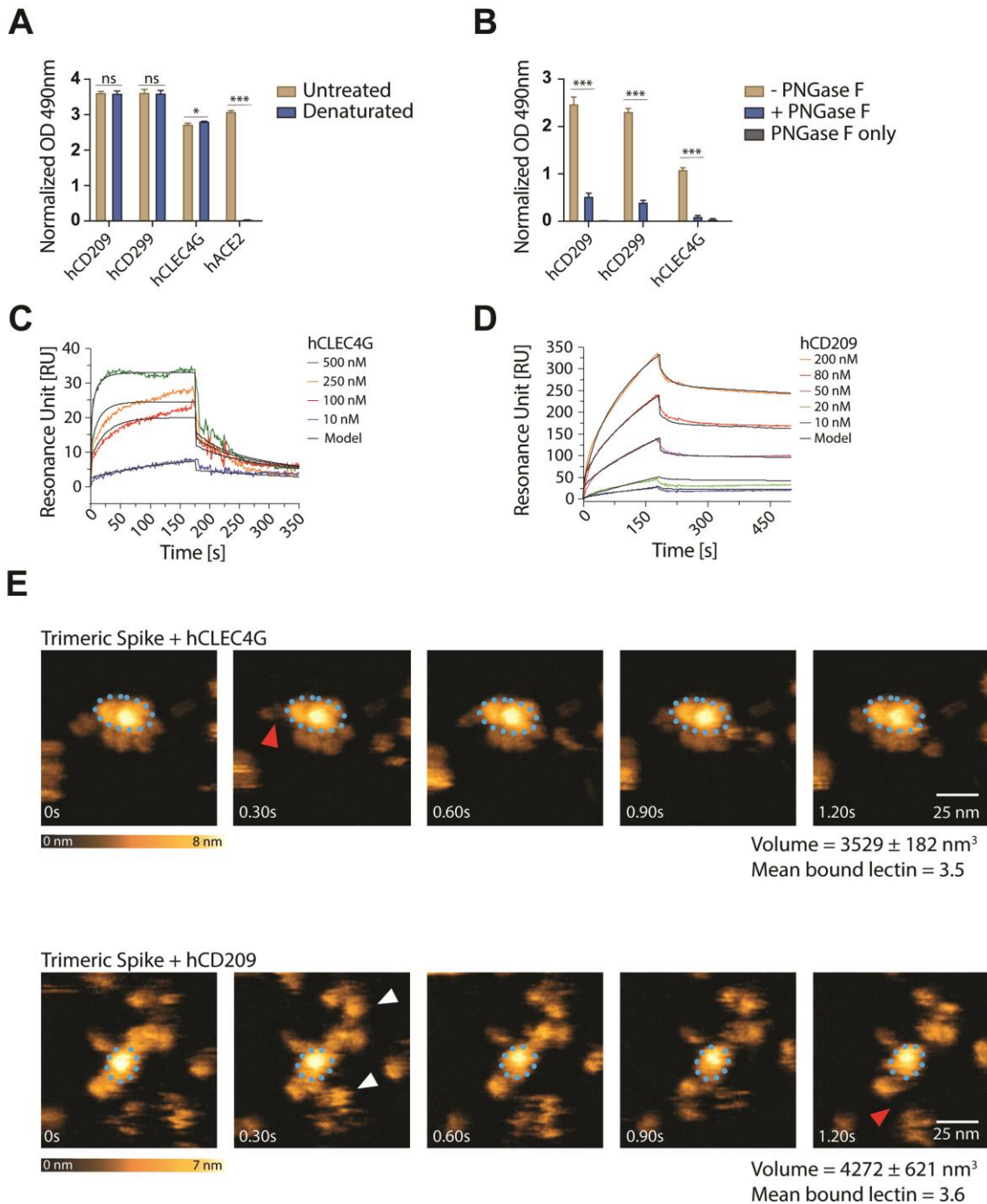
923

924

925 **Figure 3. Single molecule, real time imaging of lectin-Spike binding.**

926 (A) Schematic overview of single molecule force spectroscopy (SMFS) experiments
927 using full-length trimeric Spike coupled to an atomic force microscopy (AFM) cantilever
928 tip and surface coated murine Clec4g-Fc or CD209c-Fc. Arrow indicates pulling of
929 cantilever. (B) Representative force traces showing sequential bond ruptures in the
930 SMFS experiments. Measured forces are shown in pico-Newtons (pN). (C)
931 Experimental probability density function (PDF) of unbinding forces (in pN) determined
932 by SMFS (black line, measured data). The three distinct maxima fitted by a multi-
933 Gaussian function reveal rupture of a single bond (blue dotted line), or simultaneous
934 rupture of 2 (red dotted line) and 3 (green dotted line) bonds, respectively. (D) SMFS-
935 determined binding probability for the binding of trimeric Spike to Clec4g and CD209c.
936 Data are shown as mean binding probability \pm SD of single, double, triple or quadruple
937 bonds (N=2). (E) High speed AFM of single trimeric Spike visualizing the real-time
938 interaction dynamics with lectins. Top panel shows 5 frames of trimeric Spike alone
939 imaged on mica. Middle and bottom panels show 5 sequential frames of trimeric
940 Spike/Clec4g and trimeric Spike/CD209c complexes, acquired at a rate of 153.6 and
941 303 ms/frame, respectively. Association and dissociation events between lectin and
942 Spike are indicated by white and red arrows, respectively. The blue dotted ellipses
943 display the core of the complexes showing low conformational mobility. Color schemes
944 indicate height of the molecules in nanometers (nm). Volumes of single trimeric Spike,
945 trimeric Spike/Clec4g and trimeric Spike/CD209c complexes are indicated, as well as
946 numbers of lectins bound to trimeric Spike, averaged over the experimental recording
947 period.

Figure 4



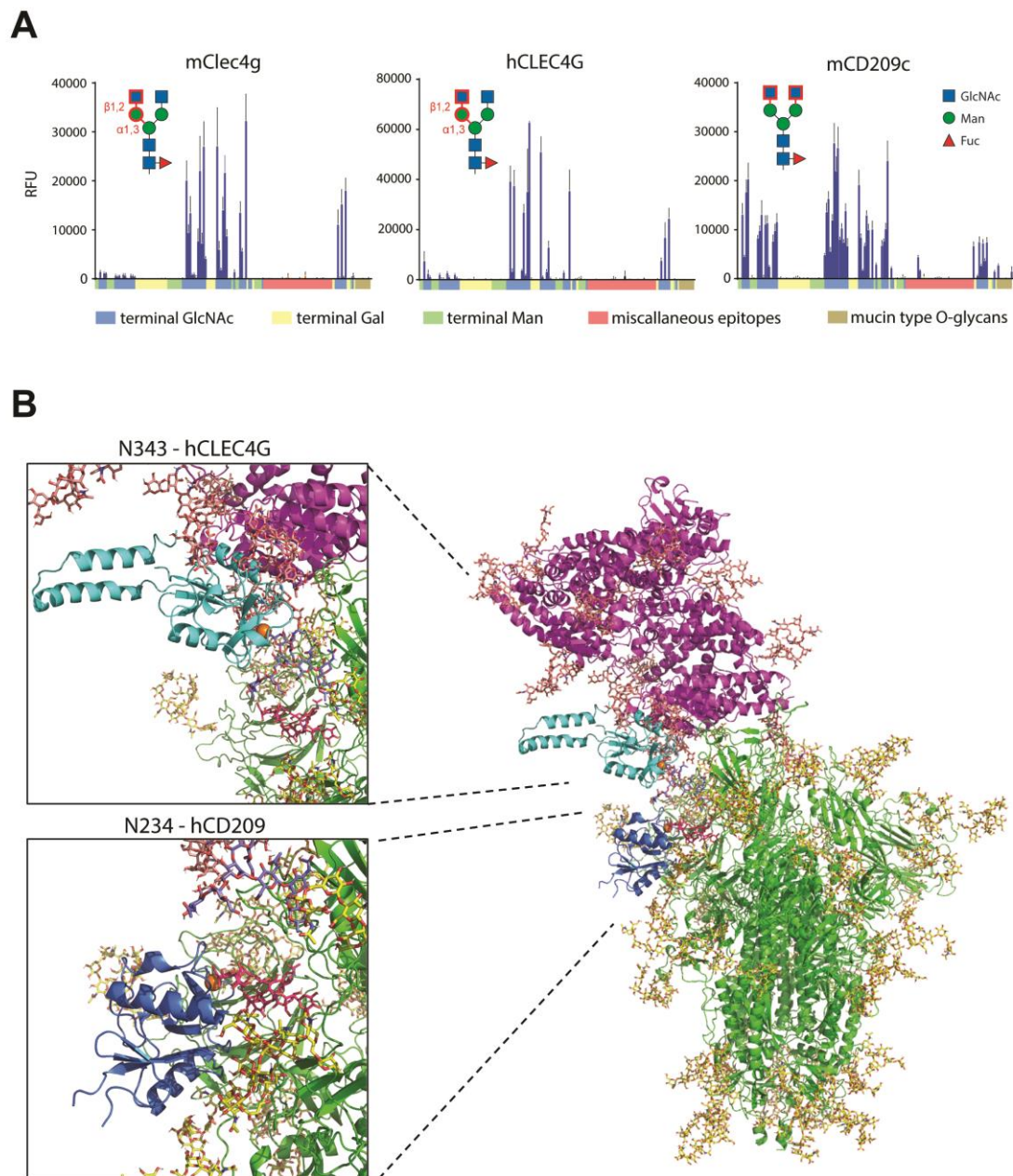
948

949 **Figure 4. Characterization of human lectin-Spike interactions.**

950 (A) ELISA analyses of human lectin-hlgG1 Fc-fusion protein (hCLEC4g, hCD209,
951 hCD299) binding to untreated or heat-denatured full-length SARS-CoV-2 Spike. A
952 human ACE2-hlgG1-Fc fusion protein (hACE2) was used to control for the complete

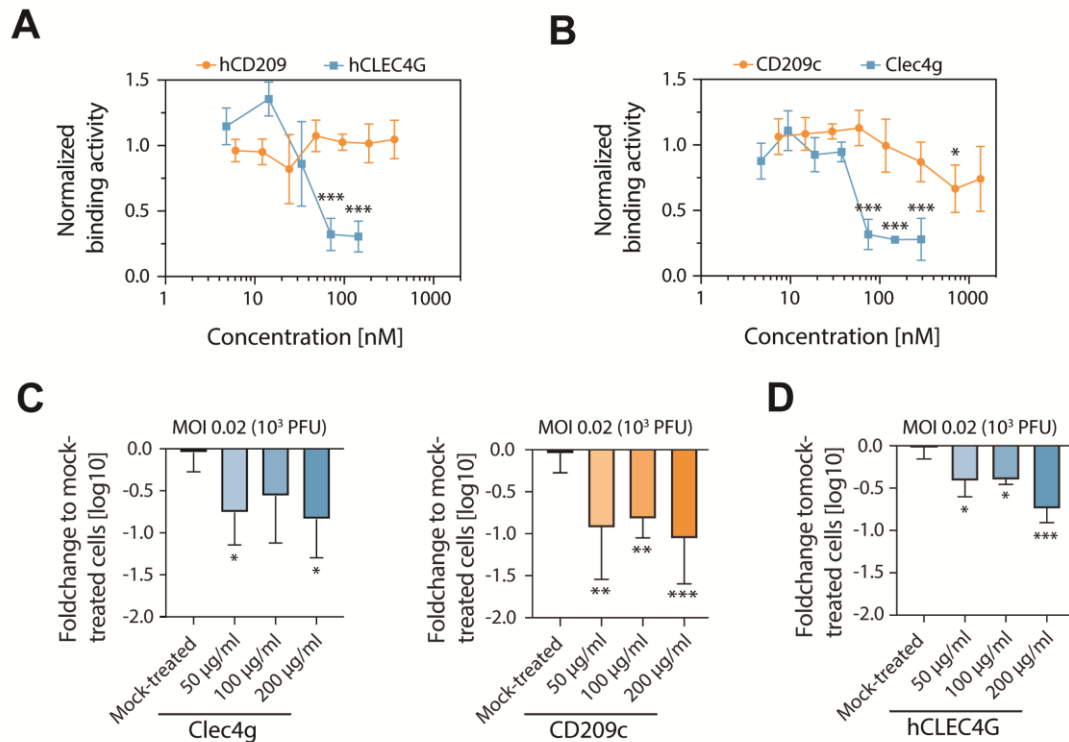
953 denaturation of Spike. Results are shown as mean OD values \pm SD normalized to a
954 BSA control (N=3). **(B)** hCLEC4g, hCD209, and hCD299 binding to full-length SARS-
955 CoV-2 Spike with or without de-*N*-glycosylation by PNGase F. “PNGase F only”
956 denotes wells that were not coated with the Spike protein. Results are shown as mean
957 OD values \pm SD normalized against the BSA control (N=3). **(C)** and **(D)** SPR analysis
958 with immobilized full-length trimeric Spike, probed with various concentrations of
959 hCLEC4G (C) and hCD209 (D). See Table 1 for kinetics values. **(E)** High speed AFM
960 of single trimeric Spike visualizing the real-time interaction dynamics with lectins. Top
961 and bottom panels show 5 sequential frames of trimeric Spike/hCLEC4G and trimeric
962 Spike/hCD209 complexes, acquired at a rate of 303 ms/frame. Association and
963 dissociation events between hCLEC4G or hCD209 and Spike are indicated by white
964 and red arrows, respectively. The blue dotted ellipses display the core of the
965 complexes showing low conformational mobility. Color schemes indicate height of the
966 molecules in nanometers (nm). Volumes of single trimeric Spike and trimeric
967 Spike/Clec4g and trimeric Spike/CD209c complexes are indicated, as well as numbers
968 of lectins bound to trimeric Spike, averaged over the experimental recording period.
969 **(A)** t-test with Holm-Sidak correction for multiple comparisons. **(B)** One-way ANOVA
970 with Tukey’s multiple comparisons; * $P < 0.05$; *** $P < 0.001$; ns: not significant.
971

Figure 5



978 standard deviation of 3 independent technical replicates. **(B)** 3D structural modelling
979 of glycosylated trimeric Spike (green with glycans in yellow) interacting with
980 glycosylated human ACE2 (purple with glycans in salmon). The CRD of hCLEC4G
981 (cyan with Ca²⁺ in orange) was modelled onto Spike monomer 3 glycan site N343
982 (complex type glycan with terminal GlcNAc in purple-blue) and the CRD of hCD209
983 (dark blue with Ca²⁺ in orange) was modelled onto the Spike monomer 3 glycan site
984 N234 (Oligomannose structure Man9 in red). Structural superposition of CLEC4G and
985 ACE2 highlights sterical incompatibility.
986

Figure 6



987

988 **Figure 6. Functional determination of lectin-Spike binding in SARS-CoV-2**

989 **infections. (A) and (B)** Binding activity of the full-length trimeric Spike coupled to an

990 AFM cantilever tip to the surface of Vero E6 cells in the presence of (A) hCLEC4G and

991 hCD209 or (B) mouse Clec4g or murine CD209c, probed at the indicated

992 concentrations in SMFS experiments. A definite decrease in binding was observed at

993 concentrations of 37 – 75 nM for Clec4g and 33 – 71 nM for hCLEC4G. Data are

994 normalized to the untreated control and shown as mean \pm SD (N=4). **(C)** Infectivity of

995 mouse Clec4g or CD209c and **(D)** hCLEC4G pre-treated SARS-CoV-2 virus in Vero

996 E6 cells. Viral RNA was measured with qRT-PCR 15 hours after infection with 0.02

997 MOI (10^3 PFUs) of SARS-CoV-2. Data represent two pooled experiments for mouse

998 lectins (N=5-6) and one experiment for hCLEC4g (N=3) and are presented as fold

999 changes of viral loads over mock-treated controls (mean log10 values \pm SD). (A) - (D)

1000 ANOVA with Dunett's multiple comparisons test with the mock-treated group; *P<0.05;

1001 **P<0.01; ***P<0.001.

1002

1003

	SPR			AFM	
	$k_{a,1}$ [M ⁻¹ s ⁻¹]	$k_{d,1}$ [s ⁻¹]	$K_{d,1}$ [M]	k_{off} [s ⁻¹]	x_{β} [nm]
Clec4g	$6,17 \times 10^4$	0,0997	$1,62 \times 10^{-6}$	0.037 ± 0.007	0.55 ± 0.02
CD209c	$1,61 \times 10^4$	0,0159	$0,988 \times 10^{-6}$	0.041 ± 0.025	0.76 ± 0.03
hCLEC4G	$7,77 \times 10^4$	0,0201	$0,259 \times 10^{-6}$	0.007 ± 0.0004	0.64 ± 0.55
hCD209	$1,32 \times 10^4$	0,0316	$2,39 \times 10^{-6}$	0.008 ± 0.001	0.73 ± 0.14

1004

1005 **Table 1. Values computed for surface plasmon resonance (SPR) and atomic**
 1006 **force microscopy (AFM).**

1007 SPR. Kinetic association ($k_{a,1}$), kinetic dissociation ($k_{d,1}$), and equilibrium dissociation
 1008 ($K_{d,1}$) constants of the first binding step fitted from the bivalent analyte model,
 1009 assuming two-step binding and dissociation of the lectins to adjacent immobilized
 1010 Spike trimer binding sites under spontaneous thermodynamic energy barriers; no
 1011 reasonable fit was obtained with the simple 1:1 binding model (data not shown). AFM.
 1012 Kinetic off-rate constants (k_{off}) and lengths of dissociation paths (x_{β}) of single lectin
 1013 bonds, originating from force-induced unbinding in single molecule force spectroscopy
 1014 (SMFS) experiments and computed using Evans's (Bell, 1978; Evans and Ritchie,
 1015 1997) model, assuming a sharp single dissociation energy barrier.

1016

1017

1018

1019

1020

1021

1022

Supplementary Materials

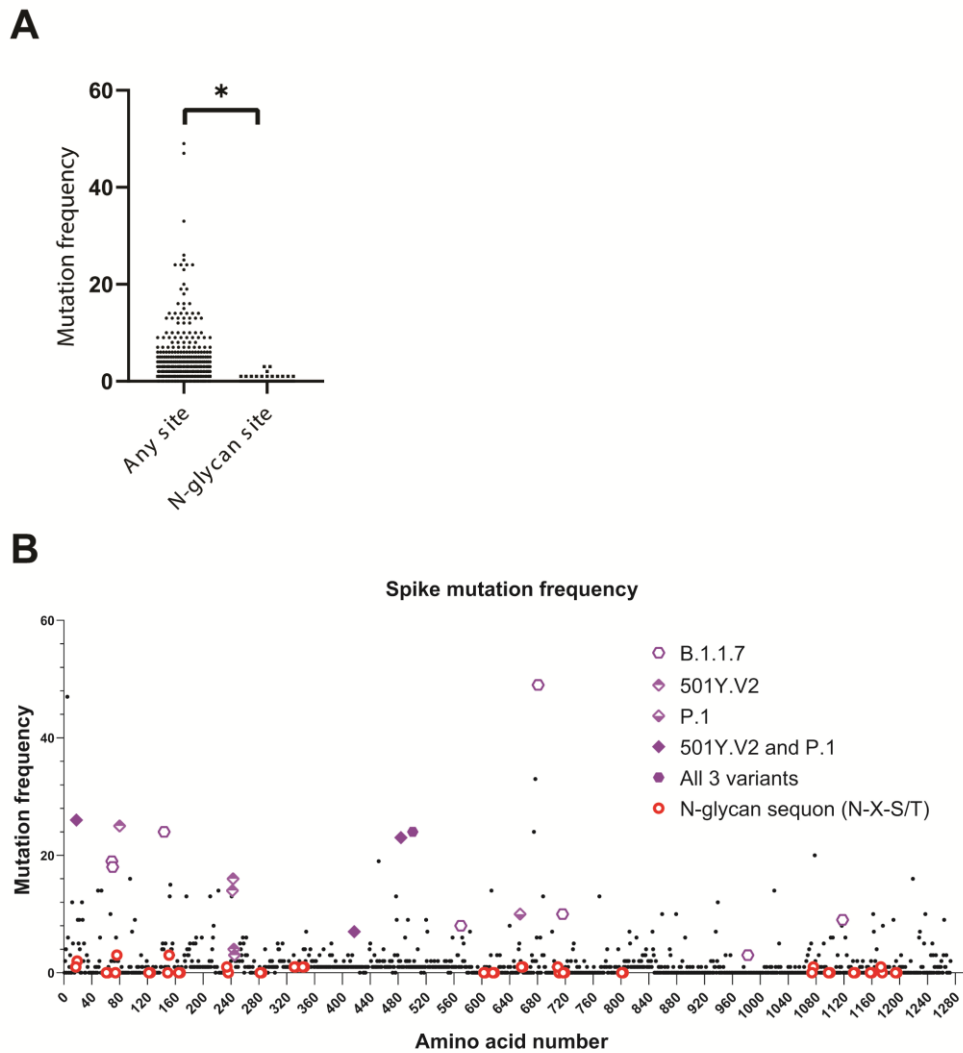
1023

1024

1025

1026

Supplementary Figure 1



1027

1028 **Figure S1. Mutation frequency of N-glycan sites on SARS-CoV-2 Spike. (A)**

1029 Among the 1273 amino acids of Spike the frequency of mutational amino acid

1030 conversion within N-glycan sequons is plotted against all other sites. **(B)** The mutation

1031 frequency of all 1273 amino acids of Spike is shown. N-glycan sequons as well as

1032 mutations harbored by the new variants B.1.1.7, 501Y.V2 and P.1 are highlighted. (A)

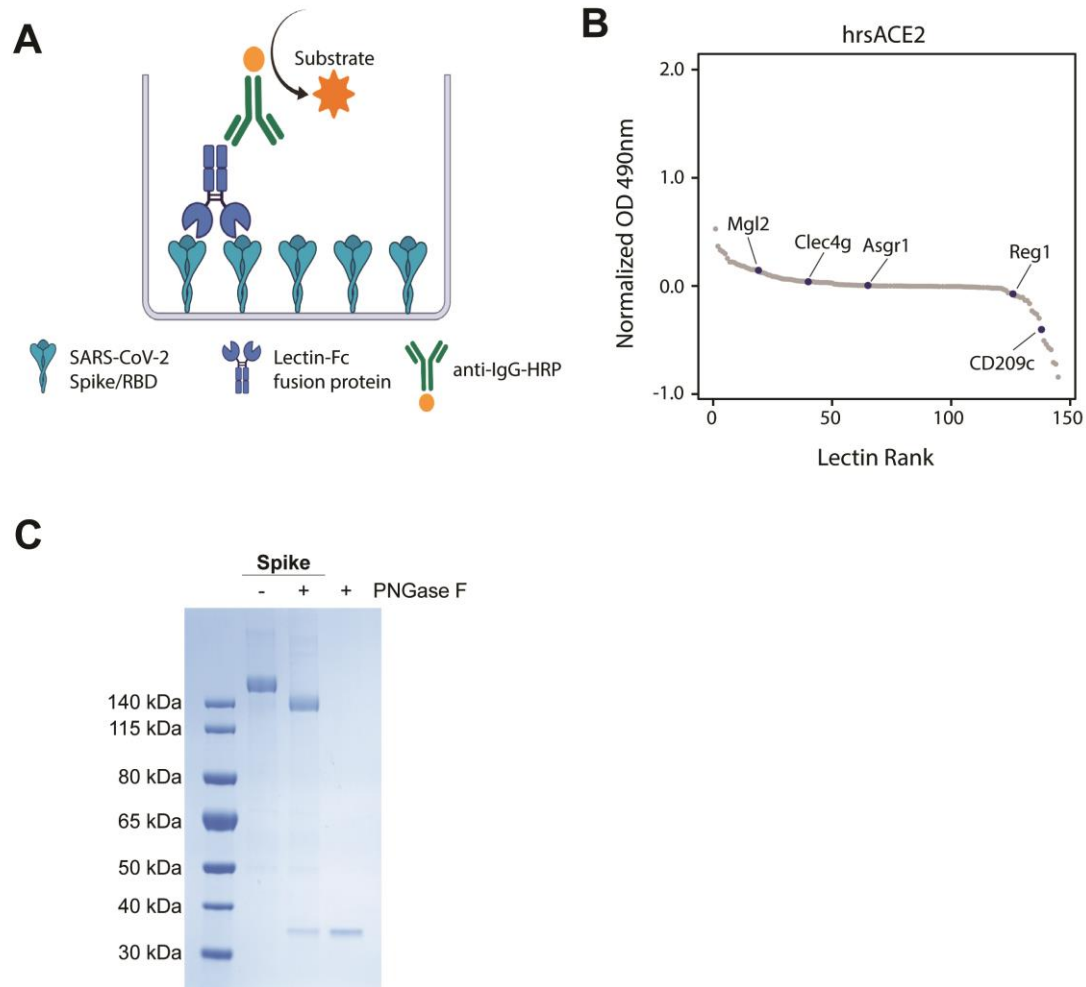
1033 Two-tailed Student's T-test, * $p < 0.05$.

1034

1035

1036

Supplementary Figure 2



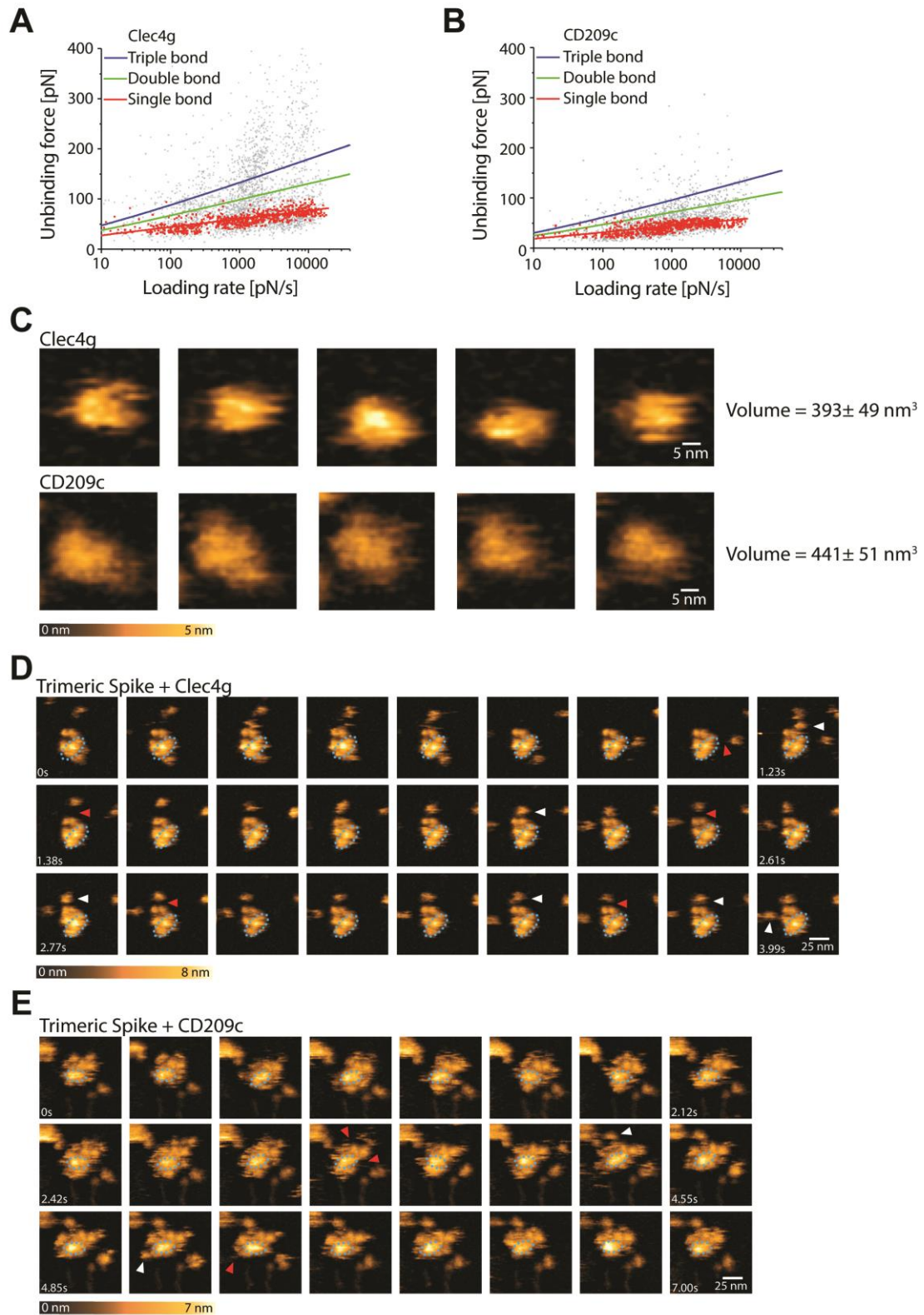
1037

1038 **Figure S2. ELISA assays to detect lectin binding.**

1039 **(A)** Schematic representation of the ELISA protocol, consisting of coating with trimeric
1040 full-length Spike or the monomeric receptor binding domain (RBD) followed by
1041 sequential incubation with lectin-Fc fusion proteins and secondary anti-IgG-HRP
1042 antibodies. The binding of lectin-Fc fusion proteins was quantified by peroxidase-
1043 dependent substrate conversion, measured by optical density (OD) at 490nm and
1044 normalized against a BSA control. **(B)** ELISA screen of the lectin-Fc library against
1045 human recombinant soluble ACE2 (hrsACE2). Results are shown as mean OD values
1046 of 2 replicates normalized against a BSA control and ranked by value. **(C)** SDS-Page

1047 of full-length Spike de-*N*-glycosylated with PNGase F and stained with Coomassie
1048 blue. A PNGase F control was added to display the size of the PNGase F protein.

Supplementary Figure 3



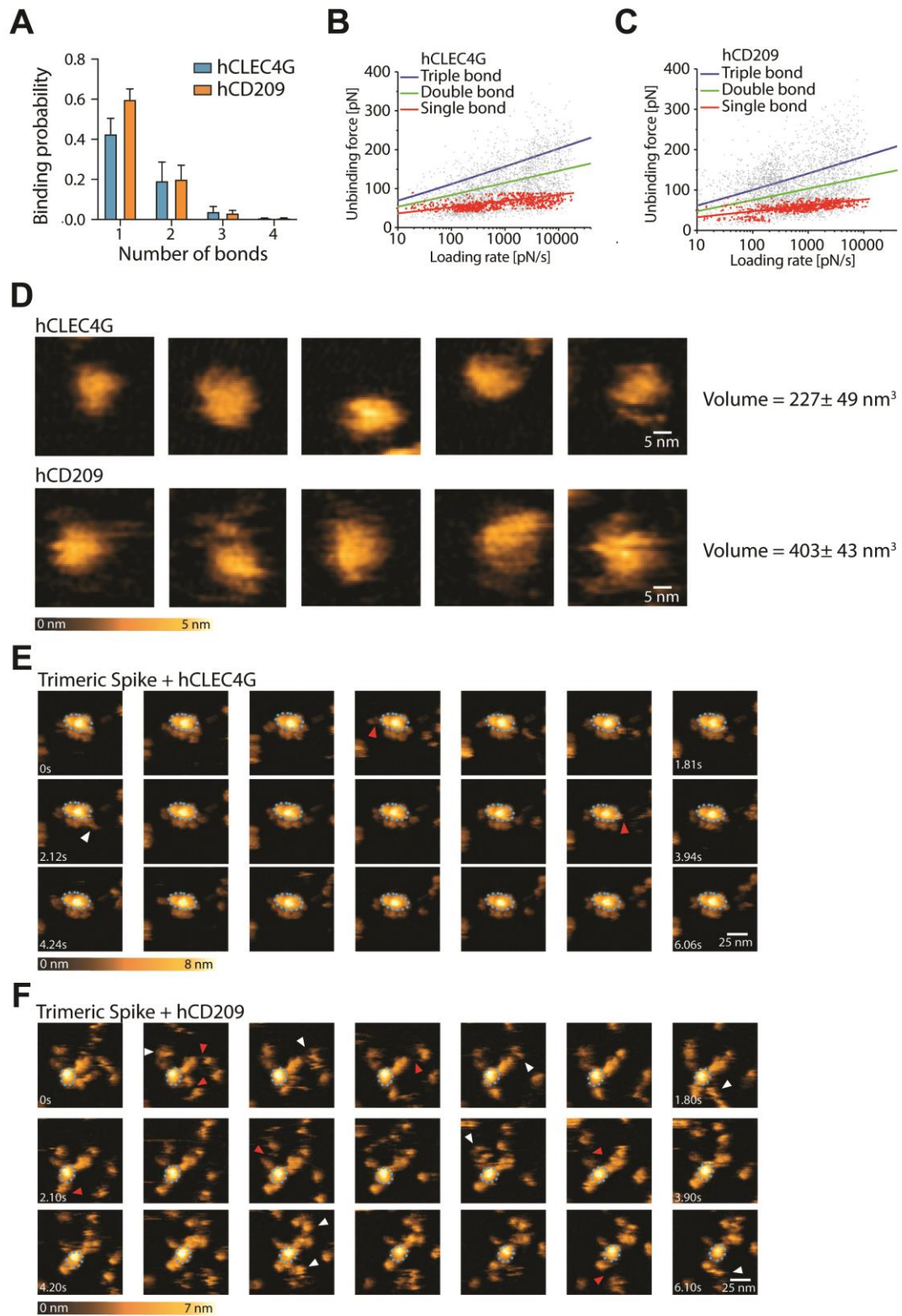
1049

1050 **Figure S3. Single molecule atomic force microscopy of a single trimeric Spike**
1051 **binding to murine Clec4g or CD209c.**

1052 (A) and (B) Unbinding forces versus loading rates for trimeric Spike dissociating from
1053 (A) Clec4g-Fc or (B) CD209c-Fc. Unbinding forces were determined from the
1054 magnitude of the vertical jumps measured during pulling of the cantilever (Fig. 3B) and
1055 individually plotted versus the respective force loading rates (equal to the pulling speed
1056 times effective spring constant) to decipher the dissociation dynamics (Table 1). A
1057 well-defined single-bond behavior of a unique monovalent bond was found (red dots)
1058 that, in line with Evans's single energy barrier model, yielded a linear rise of the
1059 unbinding force with respect to a logarithmically increasing loading rates for both (A)
1060 Clec4g and (B) CD209c. Double (green) and triple (blue) bond behaviors were
1061 calculated according to the Markov binding model using parameters derived from the
1062 single barrier model. Unbinding force values scattered between single and triple bond
1063 strengths, indicating that interactions with various glycosylation sites with different
1064 binding strengths. pN=picoNewton, pN/s = picoNewton per second. (C)-(E) High
1065 speed AFM of a single trimeric Spike visualizing the real-time interaction dynamics
1066 with lectins. (C) 5 frames of Clec4g or CD209c alone imaged on mica. (D) Sequential
1067 movie frames of trimeric Spike/Clec4g complexes, acquired at a rate of 153.6
1068 ms/frame, corresponding to Fig. 3C. (E) Sequential movie frames of trimeric
1069 Spike/CD209c complexes, acquired at 303 ms/frame, corresponding to Fig. 3C. White
1070 arrows point to lectins associating with the Spike trimer body. Red arrows indicate
1071 dissociation of lectins from the Spike trimer, highlighting positions where the lectin was
1072 bound in the previous frame. Blue dotted ellipses display low mobility regions. Color
1073 schemes indicate height in nanometers (nm).

1074

Supplementary Figure 4



1075

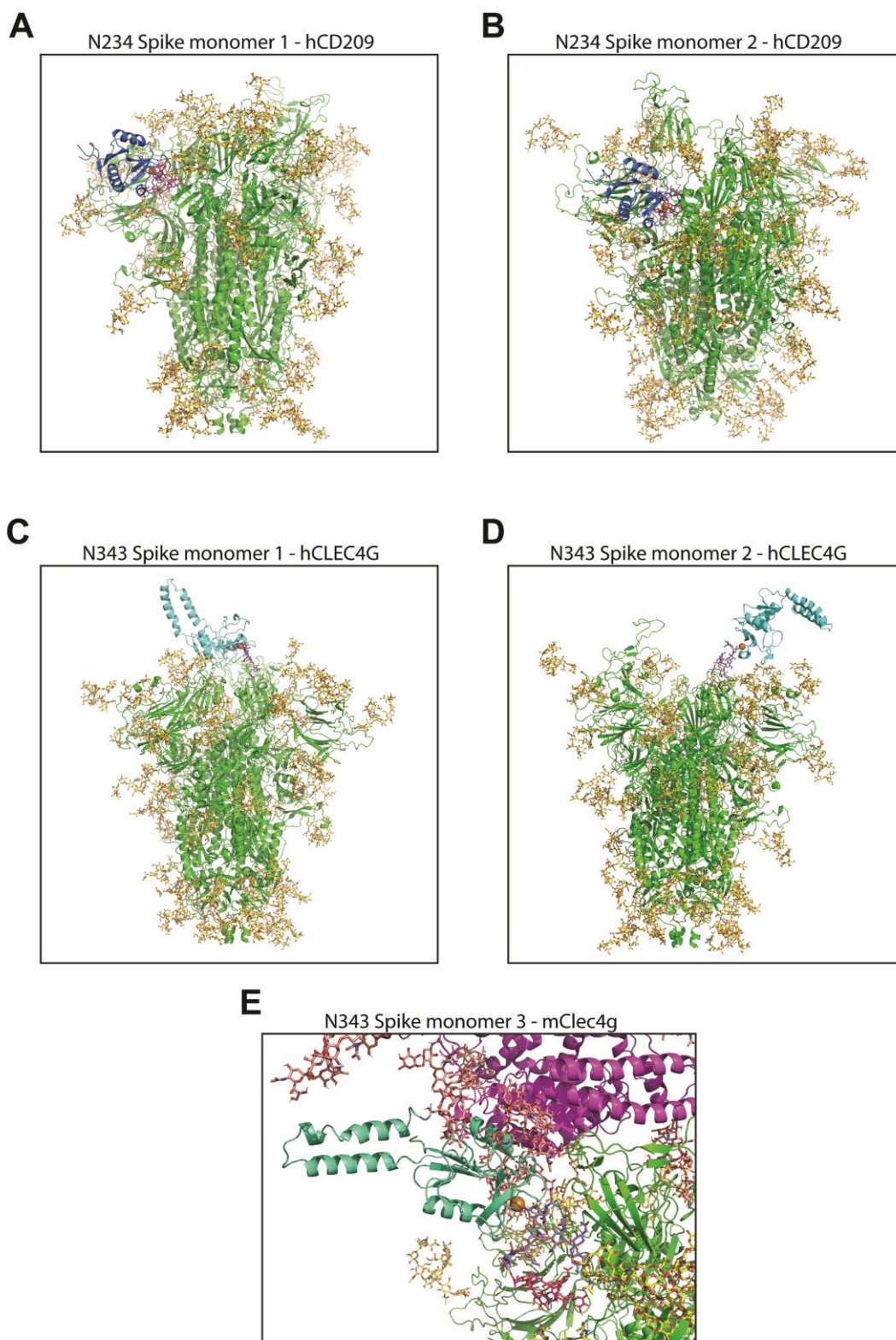
1076

1077 **Figure S4. Single molecule atomic force microscopy of a single trimeric Spike**
1078 **binding to human CLEC4g or CD209.**

1079 **(A)** Single molecule force spectroscopy (SMFS) to determine the binding probability
1080 for trimeric Spike to mica coated hCLEC4G and hCD209. Data are shown as mean
1081 binding probabilities \pm SD of single, double, triple or quadruple bonds (N=2). **(B)** and
1082 **(C)** Unbinding forces versus loading rates for a single trimeric Spike dissociating from
1083 **(B)** hCLEC4G or **(C)** hCD209. Unbinding forces were determined from the magnitude
1084 of the vertical jumps measured during pulling (Fig. 3B) and individually plotted vs. their
1085 force loading rates (equal to the pulling speed times effective spring constant) to
1086 assess the dissociation dynamics (Table 1). Single bond interactions (red dots) were
1087 fitted using the Bell-Evans single barrier model (red line). A well-defined single-bond
1088 behavior of a unique monovalent bond was found (red dots) that, in line with Evans's
1089 single energy barrier model, yielded a linear rise of the unbinding force with respect to
1090 a logarithmically increasing loading rate for both **(B)** hCLEC4g and **(C)** hCD209.
1091 Double (green) and triple (blue) bond behaviors were calculated according to the
1092 Markov binding model using parameters derived from the single barrier model.
1093 Unbinding force values scattered between single and triple bond strengths, indicating
1094 that they arise from multiple interactions with various glycosylation sites.
1095 pN=picoNewton, pN/s = picoNewton per second. **(D)-(F)** High speed AFM of a single
1096 trimeric Spike visualizing the real-time interaction dynamics with lectins. **(D)** 5 frames
1097 of hCLEC4g or hCD209 alone imaged on mica. **(E)** Sequential movie frames of trimeric
1098 Spike/hCLEC4g complexes, acquired at a rate of 303 ms/frame, corresponding to Fig.
1099 4E. **(F)** Sequential movie frames of trimeric Spike/hCD209 complexes, acquired at
1100 153.6 ms/frame, corresponding to Fig. 4E. White arrows point to lectins associating
1101 with the Spike trimer body. Red arrows indicate dissociation of lectins from the Spike

1102 trimer, highlighting positions where the lectin was bound in the previous frame. The
1103 blue dotted ellipses display low mobility regions. Color schemes indicate height in
1104 nanometers (nm).

Supplementary Figure 5



1105

1106

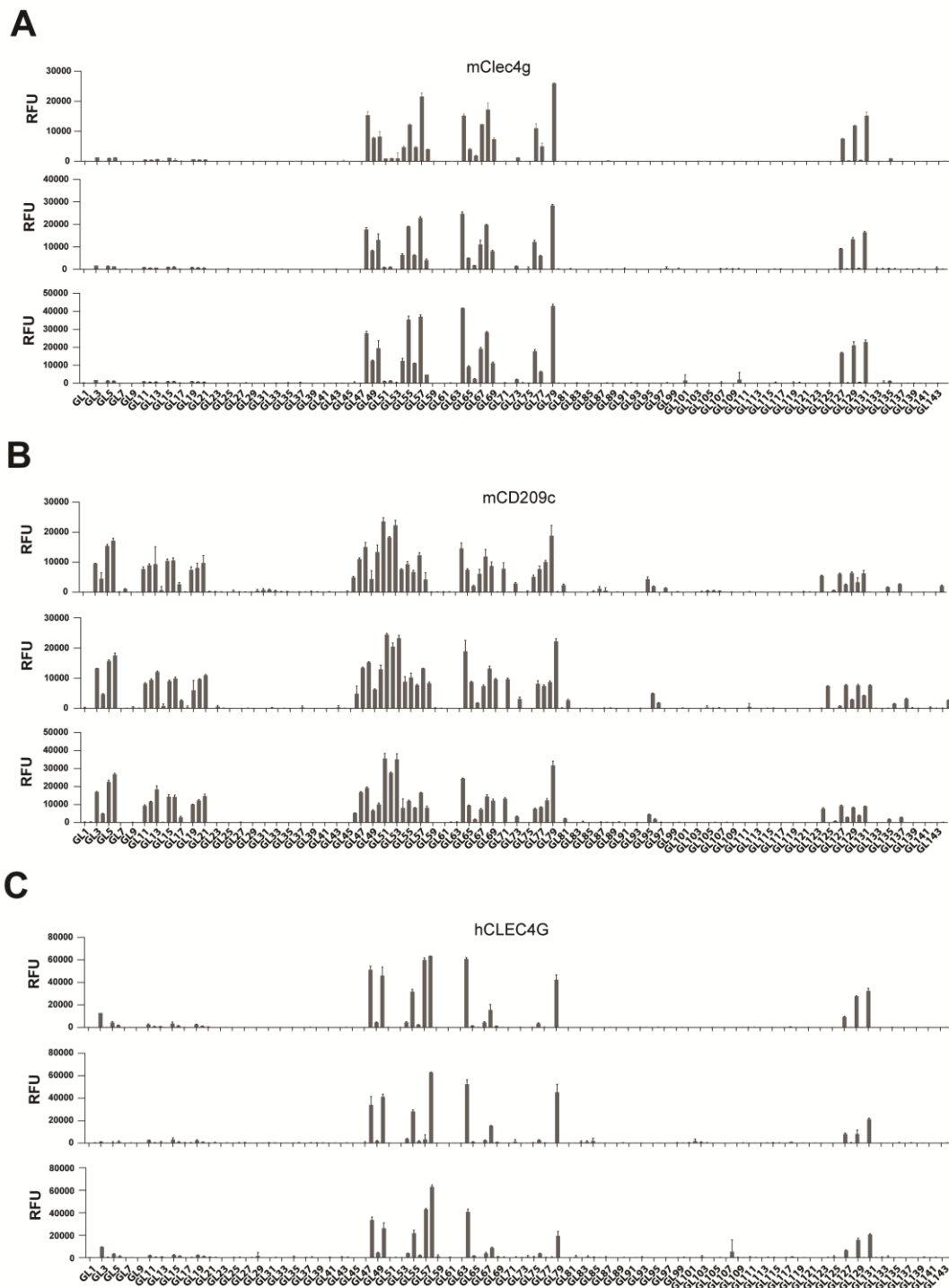
1107

1108 **Figure S5. Structural modelling of lectin-Spike interactions.**

1109 (A) and (B) 3D structural modelling of glycosylated trimeric Spike (green with glycans
1110 in yellow) interacting with the CRD of hCD209 (dark blue with Ca²⁺ in orange). The
1111 model shows the (A) Spike monomer 1 and (B) Spike monomer 2 glycan site N234
1112 (Oligomannose structure Man9 in red) bound to hCD209. (C) and (D) 3D structural
1113 modelling of glycosylated trimeric Spike (green with glycans in yellow) interacting with
1114 the CRD of hCLEC4g (cyan with Ca²⁺ in orange). The model shows Spike (A)
1115 monomer 1 and (B) monomer 2 glycan site N343 (complex type glycan with terminal
1116 GlcNAc in purple-blue) bound to hCLEC4g. (E) 3D structural modelling of glycosylated
1117 trimeric Spike (green with glycans in yellow) interacting with glycosylated human ACE2
1118 (purple with glycans in salmon). The CRD of mClec4g (cyan with Ca²⁺ in orange) was
1119 modelled onto Spike monomer 3 glycan site N343 (complex type glycan with terminal
1120 GlcNAc in purple-blue). Structural superposition of mClec4g and ACE2 highlights
1121 steric incompatibility.

1122

Supplementary Figure 6



1123

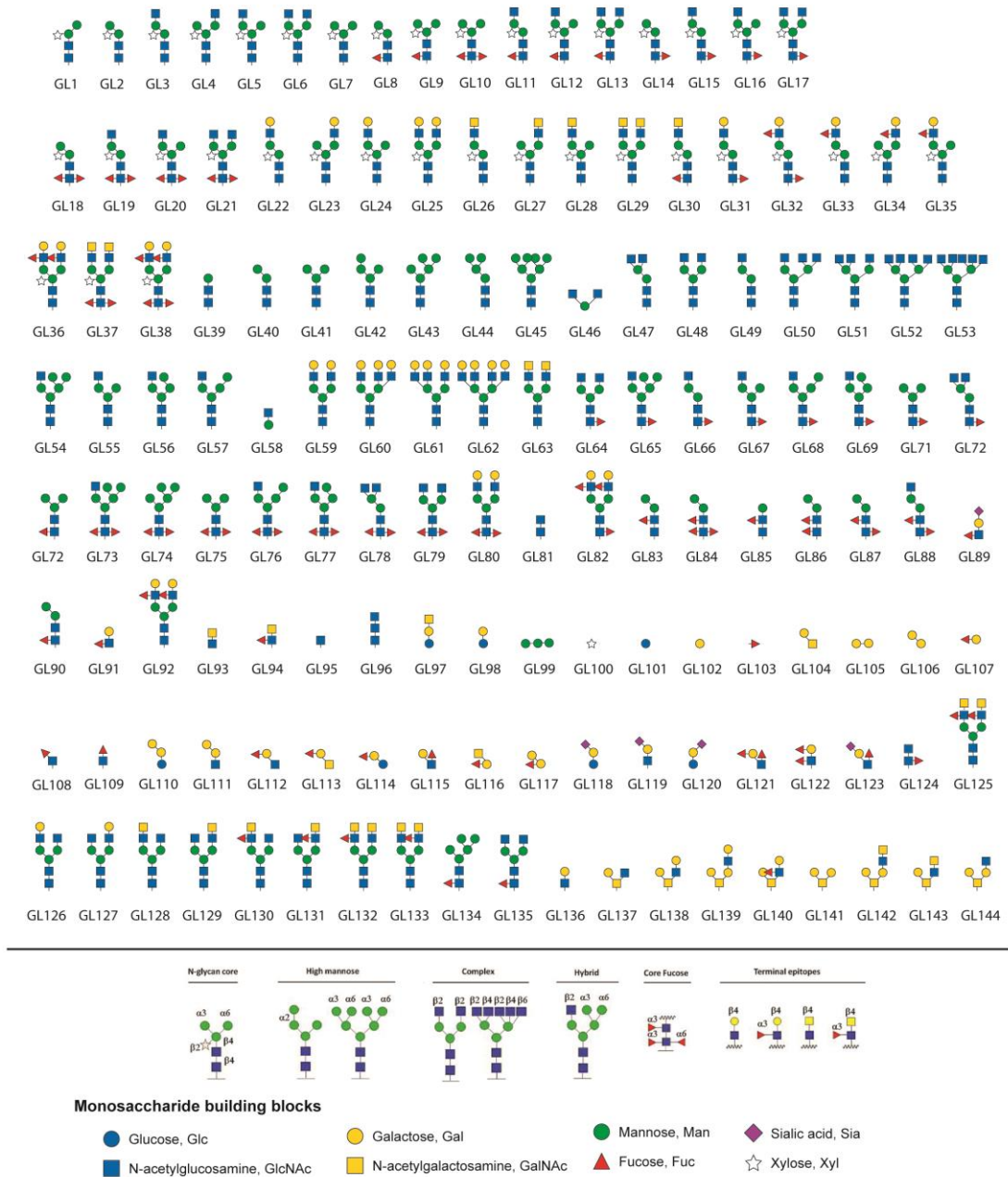
1124 **Figure S6. Glycan microarray results.**

1125 Binding of mClec4g, mCD209c and hCLEC4G to glycans spotted on the microarray.

1126 Primary data from three independent microarray measurements are shown. Each

1127 histogram shows the average values of relative fluorescence units (RFU) +/- standard
 1128 deviation. Glycan structures of GL1 to GL144 is represented in Fig S7.

Supplementary Figure 7



1129

1130 **Figure S7. Representation of the Glycan microarray.**

1131

1132

1133 **Table S1. Overview of carbohydrate recognition domains (CRDs) used for the**
1134 **lectin library**

1135 This table presents a list of CRDs expressed and purified as Fc-fusion proteins for the
1136 lectin library. Information displayed are the lectin name, the family and in the case of
1137 C-type lectins, the group and group name the CRD belongs to. CRDs from lectin that
1138 contain several CRDs are distinguished by suffix numbers. CTL = C-type lectin

1139

1140

1141 **Table S2. Glycosylation of SARS-CoV-2 Spike and RBD**

1142 Relative abundance of all measured glycans in % of all glycans present at each
1143 position. Glycans are grouped in families consisting of designated glycan features.

1144

1145

1146 **Table S3. ELISA screen of the lectin-Fc library against SARS-CoV-2 Spike, RBD**
1147 **and hrsACE2**

1148 Results from the ELISA screens of the lectin-Fc library against indicated targets. Data
1149 displayed per lectin is mean and standard deviation (SD) (n=2). SD=NA indicates that
1150 mean was calculated from a single replicate only.

1151

1152 **Table S4. Glycan microarray replicates of mClec4g, mCD209c, and hCLEC4G.**

1153 Represented is the average (Avg) and standard deviation (SD) of the relative
1154 fluorescence units (RFU) measured among 4 replicated spots ($n = 4$). The glycan
1155 structures of GL1 to GL144 are illustrated in Fig. S7.

1156

1157 **Movie S1.** High speed AFM of single trimeric Spike visualizing the real-time interaction
1158 dynamics with mClec4g acquired at a rate of 153.6 ms/frame.

1159 **Movie S2.** High speed AFM of single trimeric Spike visualizing the real-time interaction
1160 dynamics with mCD209c acquired at a rate of 303 ms/frame.

1161 **Movie S3.** High speed AFM of single trimeric Spike visualizing the real-time interaction
1162 dynamics with hCLEC4G acquired at a rate of 303 ms/frame.

1163 **Movie S4.** High speed AFM of single trimeric Spike visualizing the real-time interaction
1164 dynamics with hCD209 acquired at a rate of 303 ms/frame.

1165

1166

1167